Spring 2017

Modification of Deposition Process Parameters for Uniform Indium Layer Deposition

Isaac Butt
Old Dominion University

MODIFICATION OF DEPOSITION PROCESS PARAMETERS FOR UNIFORM INDIUM LAYER DEPOSITION

by

Isaac Butt
B.Tech. May 2014, Jawaharlal Nehru Technological University, India

A Thesis Submitted to the Faculty of
Old Dominion University in Partial Fulfillment of the
Requirements for the Degree of

MASTER OF SCIENCE

ELECTRICAL AND COMPUTER ENGINEERING

OLD DOMINION UNIVERSITY
May 2017

Approved by:

Sylvain Marsillac (Director)

Christian Zemlin (Member)

Chung Hao Chen (Member)

ABSTRACT

MODIFICATION OF DEPOSITION PROCESS PARAMETERS FOR UNIFORM INDIUM LAYER DEPOSITION

Isaac Butt
Old Dominion University, 2017
Director: Dr. Sylvain X. Marsillac

The need for more efficient light to energy converting cells has long been a subject of research and development. With abundant availability of solar energy that the earth receives, the photovoltaic industry has sought materials that could serve the purpose of great energy conversion. The photovoltaic industry is mainly dominated by Silicon owing to its abundant availability, reliability and economic cost. However, due to limitations on efficiency improvements, some focus has shifted toward III-V based solar cells with a great potential for attaining higher efficiency and multi-junction applications. However, the cost of the III-V materials is extremely high due to the cost of the raw materials, the need for a lattice-matched substrate for single crystal growth, and complex growth processes. Research groups have investigated direct non-epitaxial growth of thin poly-crystalline films using a MOCVD process and VLS growth on cheaper substrates [1,2]. To do so, it is important to develop a planar reaction template for the group III metal, which will prevent de-wetting of the seed layer from the substrate during growth. In this thesis, we study various deposition parameters (substrate, deposition rate, structure…) that improve the de-wetting of an Indium layer as a template for future III-V virtual substrate.

ACKNOWLEDGEMENTS

I would like to thank my committee chair, Dr. Sylvain X. Marsillac, for his enormous support, patience and guidance in every step. Thank you for being so flexible and patient with me though every challenge I experienced in the past year. I am extremely grateful for all the knowledge I have gained from working on your highly skilled research team. Dr. Marsillac is the best mentor any student could ever have. I would also like to thank Grace Rajan and Shankar Karki for their support and continued guidance and training.

I would also like to thank Dr. Christian Zemlin and Dr. Chung Hao Chen for serving on my thesis committee. I am grateful for all the opportunities and knowledge this program has provided.

TABLE OF CONTENTS

LIST OF TABLES

Table Page

LIST OF FIGURES

Figure Page

CHAPTER 1

INTRODUCTION

1.1 NEED FOR MORE EFFICIENT SOLAR CELLS

Much of the global energy demand is supplied by burning fossil fuels such as coal, petroleum and natural gas. The increasing energy demand has caused an upward trend in cost, and the need for cleaner energy can be a powerful motivation for the development of alternative energy sources. This can reduce the relative costs of making a broader range of technologies but also to make more efficient photovoltaic cells. A photovoltaic cell is a semiconductor device (a p-n junction) that converts sunlight in the form of photons to electricity. When the photons emitted from the sun hit the cell, electron-hole pairs are generated if the energy of the incident photon is higher than the bandgap of the material. These light generated e-h pairs are separated and collected by appropriate electrodes. Multi-junction solar cells are formed by stacking multiple cells with different bandgap energies to maximize the absorption of photons.

1.2 ADVANTAGES OF III-V MATERIALS

The distance between the energy bandgap of the solar cell and energy of the photon results in a loss of energy; thus, it is important to develop wider bandgap materials. III-V group compounds have several material characteristics to make it the most efficient photovoltaic material available today, and it provides wide flexibility of the range of materials that can be combined. Several compounds can interact strongly with light due to their nature of being able to retain direct bandgaps and having high corresponding absorption coefficients.

Thus, III-V materials are a class of materials with extreme potential and therefore feature most of the opto-electronically efficient semiconductors [2]. Many questions could be asked before deciding on which material to work. The first question is about the choice of material to be picked out of the 12-selected group. The second question would be about the suitable procedure of growth for the chosen material. Other parameters of interest are lattice constant, bandgap, melting point, structural characteristics, etc. These were investigated while considering these materials for research. Lattice constant is related to the physical structure and dimension of the unit cell in the crystal lattice, while the bandgap is related to the difference between the top of the valence band and the bottom of the conduction band in semiconductors. The melting point of each compound was also considered to figure out the suitable compound that could be used with a relatively low melting point. The coefficient of thermal expansion was also considered to understand the degree of expansion of the compound over the change in temperature.

1.3 Thesis Objective

III-V materials have demonstrated excellent characteristics with high efficiencies for single and multi-junction cells and for a wide variety of optoelectronic devices. InP and InAs are gaining attention because of their excellent properties that enable them to be used for a wide range of applications. InP has an ideal bandgap of 1.34 eV and a low surface recombination velocity, making it ideal for polycrystalline applications. Extreme radiation tolerance of the material also makes it suitable for space applications. On the other hand, InAs has a lower bandgap of 0.36 eV and a high electron mobility of around 10^3 V/s, making it suitable for fabricating photodetectors and for electron quantum wells. However, cost of the III-V materials is extremely high due to the cost of the raw materials, the need for a lattice matched substrate for single

crystal growth and complex growth processes. Research groups have investigated direct non-epitaxial growth of thin polycrystalline films using a metal organic chemical vapor deposition (MOCVD) process and vapor liquid solid (VLS) growth on cheaper substrates [1,2]. For VLS, it is important to develop a planar reaction template for the group III metal that will prevent de-wetting of the seed layer from the substrate during growth. In this study, we looked at the fundamental properties of the III-V materials and the possibility of achieving successful VLS growth. Considering the parameters and the different techniques that could be used to be able to grow a III-V material, experiments were conducted to grow a uniform layer of Indium so as to prepare a groundwork to fabricate InP, InAs, InN or InSb. The principle of wettability and the spreading of liquid metal on a solid surface was studied with the help of surface thermodynamics. The experiments were carried out to grow a uniform layer of Indium as a template for VLS growth on different substrates like soda lime glass (SLG), molybdenum foil (Mo foil) and silicon wafer with native oxide (native silicon). Different deposition processes and structures were optimized to achieve the best uniform growth. Experimental details, results and conclusions were drawn from each experiment and are reported in this thesis.

CHAPTER 2

LITERATURE REVIEW

2.1 PROPERTIES OF III-V MATERIALS

III-V materials and devices have immense applications in opto-electronic and photovoltaic systems. III-V compound semiconductors are formed due to the bonding of one of the group III elements such as aluminum, gallium or Indium with one of the group V elements such as nitrogen, phosphorous, arsenic or antimony. Their bandgap varies from 0.17 eV for Indium Antimonide to 6.01 eV for Aluminum Nitride. In this section, the fundamental properties of III-V materials such as structural, physical or electrical properties are discussed.

Aluminum Nitride (AlN)

Aluminum nitride (AlN) is a nitride of aluminum. It has a wide bandgap (6.01-6.05 eV), making it suitable for ultraviolet optoelectronics. The lattice constant of AlN at 300K is a = 3.11 Å, c = 4.98 Å. The band structure differs from that of most other III-V group compounds since it crystallizes in the wurtzite lattice. Aluminum nitride is (typically) a covalently bonded material and has a hexagonal crystal structure that is isomorphic.

AlN has excellent properties such as high thermal conductivity, spread out bandgap, and thick transparency of ultraviolet light. AlN is non-reactive with other semiconductor processes and gases and possesses good dielectric properties and has a low thermal expansion coefficient closer to Silicon. The melting point of aluminum nitride is 2,200 °C. Thermal conductivity is

the most remarkable property exhibited by AlN. The thermal conductivity exceeds that of copper even at a moderate temperature of about 200°C. AlN has a unique application as substrates for high power assemblies of microelectronic components due to its high conductivity along with high volume resistivity and dielectric strength. The properties mentioned above increase the suitability of AlN for use in LEDs in the ultraviolet spectrum and prove its great scope for high-power electronic devices for the next generation. To develop the potential use of nitride semiconductors there has always been a need for high-quality AlN crystal.

Aluminum Phosphide (AlP)

Aluminum phosphide is an inorganic compound that is highly toxic. The crystal structure of AlP is called zinc blende crystal structure. AlP is the chemical formula for Aluminum Phosphide, which is used as a fumigant agent and as a semiconductor with a wide bandgap. The lattice constant of AlP at 300k is a = 5.451Å. When AlP reacts with moisture it gives phosphine, which is a poisonous gas and is highly flammable. Generally, phosphine spontaneously ignites upon contact with surrounding gases present in the air. Excess water can be used to control the phosphine fire to avoid any surrounding combustible material from being ignited. AlN has a high melting point of 2530°C. When AlN is heated to high temperatures of decomposition it is prone to emit oxides of toxic phosphorus. AlP can be applied in semiconductor applications and insecticide.

Aluminum Arsenide (AlAs)

Aluminum arsenide is a semiconductor material having a zincblende crystal structure similar to AlP. Aluminum arsenide and gallium arsenide have almost the same lattice constants. The lattice

constant of AlAs is a = 5.66 Å with a bandgap of 2.16 eV. The melting point of AlAs is 1740 °C. The applications of AlAs are spread in various areas such as solar cells, devices with quantum well and optoelectronic devices that are growing technologies for the past decade. The use of AlAs is extensively observed in high-electron-mobility transistors used in everyday semiconductor IC's. However, decomposition of aluminum arsenide will produce hazardous arsenic gas and arsenic fumes.

Aluminum Antimonide (AlSb)

Aluminum antimonite is also one of the semiconductor compounds of the group III-V in the periodic table. The crystal structure of AlSb is a zinc blende. The lattice constant of AlSb is a = 6.135Å with a bandgap of 1.58 eV. AlSb has a relatively low boiling point of 1060 °C. An important property of AlSb is its nature to form alloys with other III-V semiconductor materials such as arsenic or gallium to produce aluminum arsenic antimonide, aluminum gallium antimonide and aluminum Indium antimonide respectively. Like aluminum phosphide (AlP), AlSb is highly flammable due to its nature to form ($Sb3^-$) ion. Aluminum antimonide finds applications in two major areas: optical fiber technology in electro-optical devices and in the field of medical science or characterization using X-ray and Gamma-ray radiation detection.

Gallium Nitride (GaN)

Gallium nitride is often used in laser technology. Gallium nitride has a Wurtzite structure like AlN. It has a lattice constant of a = 3.186 Å, c = 5.186 Å. The bandgap of GaN is 3.4 eV. The lasers produce a range of wavelengths between 360 to 480 nanometers; therefore, the color of these wavelengths is perceived by the human eye to be blue or violet. The melting point of GaN

is 2500 °C. Gallium Nitride is the best among all other gain mediums for semiconductor lasers. Fascinatingly, violet light can be produced with the help of GaN semiconductor lasers without the need for doubling of frequency, which is remarkable. The process of emissions of blue or violet radiation is by using high quality GaN crystals to form the p-n junction then pumping the laser with electric current. The prime application of the GaN laser is in storage of data. GaN was the key component used as a laser emitting a 405 nm wavelength, which is used in high definition Blu-ray disc data storage/recording. Other applications of the GaN laser are in telecommunications, daily use of electronic equipment, monitoring of the environment and of course in information technology as discussed briefly.

Gallium Phosphide (GaP)

A gallium phosphide semiconductor has a pale orange color. It has a zinc blende crystal structure with an indirect bandgap of 2.26 eV, which also is a great explanation for its pale orange color. The lattice constant of GaP is a = 5.45 Å. This compound has a boiling point of 1477 °C. It is observed that single crystal wafers that are not doped are clear orange in color but the wafers however, that are doped strongly look darker due to absorption of free carrier. Gallium phosphide does not dissolve in water and is completely odorless. Tellurium or sulfur are used as dopants to obtain n-type semiconductors and Zinc is used to form p-type semiconductor. Gallium phosphide is extensively used in manufacturing of LEDs at a very low-cost. The colors such as red, orange, and green can be produced using these GaP (LEDs) with variation of brightness from low to medium. On the down side, the lifetime of these LEDs is relatively short with a higher current and it is very temperature sensitive. This can be used alone with gallium arsenide phosphide or even by itself, which makes it unique. At a wavelength of 555 nanometers

green light can also be emitted with pure gallium phosphide.

Gallium Arsenide (GaAs)

Gallium arsenide is a type III-V semiconductor with a zinc blende crystal structure. It has several advantages such as high electron mobility and, compared to silicon, it has a high-saturated electron velocity. Transistors made with gallium arsenide can function at high frequencies over 250 GHz. The lattice constant of GaAs is a = 5.65 Å with a bandgap of 1.42 eV. Gallium Arsenide has a melting point of 1238 °C. Because of their wide bandgap, gallium arsenide devices are not sensitive to heat. These devices typically also happen to have less noise compared to silicon devices, especially at high operating frequencies. The applications of gallium arsenide are in the field of microwave technology where GaAs can be used to manufacture devices such as monolithic microwave integrated circuits and microwave frequency and in the manufacturing of integrated circuits, infrared light-emitting diodes, solar cells, laser diodes and optical windows. GaAs can emit light with high efficiency because it has a direct bandgap unlike many other semiconductors. Being a direct bandgap material, it is resistant to radiation damage enabling its use in optical windows and space electronics in high power applications.

Gallium Antimonide (GaSb)

Gallium antimonide (GaSb) is a semiconductor made of gallium and antimony belonging to the III and V semiconductor family respectively. It has a crystal structure known as sphalerite, which is similar to a diamond structure. The lattice constant of GaSb is a = 6.09Å. The melting point of GaSb is considerably low at 712 °C. The unique lattice structure of GaSb permits it to be used in various sophisticated semiconductor applications. For example, the first ever dual mode passive and active infrared camera chip was made of gallium antimonide and Indium arsenide.

Other uses of gallium antimonide in the electronics industry are in the manufacturing of infrared detectors, infrared LEDs, transistor lasers and thermo-photovoltaic systems.

Indium Nitride (InN)

Indium nitride is a semiconductor material that has a wurtzite crystal structure. It has a potential application in high-speed electronics and solar cells. Lattice parameters of the wurtzite crystalline structure of InN are a = 3.54 Å and c = 5.186 Å. The bandgap of Indium nitride is 1.97 eV. InN has a melting point of 1,100 °C. At liquid helium temperatures polycrystalline films of Indium nitride are observed to be highly superconductive or conductive. Research in developing solar cells using nitride-based semiconductors is actively going on today. Using the alloy Indium gallium nitride an optical match to the solar spectrum is obtained.

Indium Phosphide (InP)

Indium phosphide (InP) is a binary semiconductor. The zinc blende crystal structure of InP makes it almost like all the semiconductors in the III-V group. The Lattice constant of InP is a = 5.86 Å with a bandgap of 1.35 eV. The melting point of InP is 942 °C. Indium phosphide can be used in high-frequency and high-power electronics as it has a superior electron velocity. InP is also used in optoelectronics devices such as laser diodes as it has a direct bandgap unlike many semiconductors.

Indium Arsenide (InAs)

Indium arsenide is a semiconductor material made of Indium and arsenic. InAs has a zinc blende crystal structure and appears in the form of grey crystals with a cubic structure. The lattice

constant of InAs is a = 6.06 Å with an extremely low bandgap of 0.36 eV. This material has a direct bandgap. The melting point of this semiconductor material is 942 °C. Important features of InAs are for its narrow energy bandgap and high electron mobility. InAs is used to construct infrared detectors that are normally photovoltaic photodiodes for a wavelength range of 1–3.8 micrometer. It is also used for detectors that are cryogenically cooled and have low noise, but InAs detectors can also be used in high-power applications at room temperature. InAs can also be used in diode lasers.

Indium Antimonide (InSb)

Indium antimonide (InSb) is a semiconductor made of antimony and Indium, which has a zinc blende crystal structure. It is a narrow gap semiconductor with a very low bandgap of 0.17 eV. The lattice constant of InSb is a = 6.48 Å. This compound has the lowest melting point of 527 °C compared to all the other III-V group materials discussed in this thesis. Indium antimonide is also used to make detectors that have sensitive wavelength in the range of 1 and 5 micrometers. InSb is a terahertz radiation source as it is a strong photo-Dember emitter by itself. It also finds use in infrared detectors, including FLIR systems, thermal imaging cameras, in infrared astronomy and in infrared homing missile guidance systems. Photo-electromagnetic detectors or photodiodes are used to get the thermal images from detectors made from InSb. The high carrier mobility of InSb is used to build fast transistors.

Table 2.1 summarizes some important parameters of the III-V materials, including the lattice constants, the bandgap, the melting point and the coefficient of thermal expansion.

Table 2.1 Main Properties of III-V group

III-V Materials	Lattice Constant at 300k (Å)	Band gap (eV)	Melting point	Thermal. Expansion Coeff (K^{-1})
Aluminium Nitride	a = 3.11 Å, c = 4.98 Å	6.015	2,200 °C	5.30E-06
Aluminum Phosphide	5.451	2.5 (I)	2,530 °C	5.73E-06
Aluminum Arsenide	5.6605	2.16 (I)	1,740 °C	5.20E-06
Aluminum Antimonide	6.1355	1.58 (I)	1,060 °C	4.10E-06
Gallium Nitride	a = 3.186 Å, c = 5.186 Å	3.4	2500 °C	5.59E-06
Gallium Phosphide	5.45	2.26 (I)	1,477 °C	4.65E-06
Gallium Arsenide	5.6533	1.424	1,238 °C	5.73E-06
Galium Antimonide	6.0959	0.72	712 °C	7.75E-06
Indium Nitride	a = 3.54 Å, c = 5.72 Å	1.97	1,100 °C	4.00E-06
Indium phosphide	*5.86*	1.35	1,062 °C	4.60E-06
Indium Arsenide	*6.06*	0.36	942 °C	4.50E-06
Indium Antimonide	6.48	0.17	527 °C	5.37E-06

Four substrates are considered for the experiments in this thesis and their properties such as thermal expansion coefficient, melting point and lattice constant which are tabulated below in Table 2.2. Soda lime glass is used because it has good thermal expansion and since it is economically available; native silicon is used because it can withstand higher temperatures. Mo foil is also a useful substrate since it is flexible and has a high melting point.

Table 2.2 Properties of Substrates used in our experiments.

Substrates	Thermal expansion	Melting point	Lattice constant
SLG	8.60E-06	564 °C	a = 5.70 Å, c = 11.36 Å
Native Si	2.60E-06	1412°C	a = 3.57 Å
Mo foil	4.80E-06	2623°C	a = 3.147 Å
Quartz, fused silica	5.50E-07	1650°C	a = 4.913 Å, c = 5.4052

2.2 VLS GROWTH

The vapor-liquid-solid (VLS) mechanism was developed in 1964 by Wagner and Ellis to explain unidirectional whisker growth [5]. Detailed studies of the morphology and growth of silicon whiskers developed a new growth process to grow a crystal with the aid of the vapor, and the

growth mechanism is known as the vapor-liquid-solid (VLS) mechanism. A nanometer-sized metal in liquid state is used in VLS growth and can be used to grow nanowire during nanowire growth. For example, these are the basic steps involved in the VLS growth mechanism of Si nanowires using Au nanoparticles on a Si (111) substrate. The growth begins with deposition of Au nanoparticles on an oxide-free Si (111) substrate and the substrate is the placed inside the reaction zone. The temperature is increased to above the eutectic temperature of Au-Si, and Au nanoparticles are formed.

VLS GROWTH KINETICS

The growth rate mainly depends on determination of kinetic coefficients and the diameter. A metal catalyst is used to assist the VLS mechanism. This is a 1D crystal growth mechanism. Creation of whiskers, rods, and wires are a result of this creation. Around 50 years ago, 1D crystal growth was initially developed, and in 1964 the mechanism was suggested for wider use by Wagner in the Silicon industry. A schematic of the VLS mechanism is shown in Figure 2.1. The metal catalyst forms liquid alloy droplets at a high temperature by adsorbing vapor components in this mechanism. The fluctuation in temperature or vapor pressure causes further supersaturation in the alloy, which means that it results in a solution in which the equilibrium concentration is lower than the actual concentration of the components. The precipitation of the component at the liquid–solid interface is driven to achieve minimum free energy of the alloy system, hence leading to the beginning of 1D crystal growth and continues as long as the vapor components are supplied. Due to the process consisting of all three phases vapor carrying solid components, liquid components carrying catalyst alloy, and solid consisting of precipitated 1D structures, this technique is known as the VLS (Vapor liquid and solid) mechanism. The

diameter and position of the 1D structures determine the size and position of the catalyst as the liquid phase is restrained to the area of the solid phase [6]. The mechanism works at a high temperature at which the metal catalyst forms a liquid alloy. Therefore, chemical processes such as chemical vapor deposition (CVD), molecular beam epitaxy (MBE) and laser ablation (LA) occur at higher temperatures, and these are generally used in unification with the mechanism.

2.3 SURFACE THERMODYNAMICS

As discussed in the previous section, VLS mechanism refers to a crystal growth mechanism where a liquid droplet is prepared on a substrate by heating above the melting point of the material. A vapor of the substance to be grown is introduced on the substrate, which causes it to adsorb on the liquid surface and then diffuses into the droplet. This causes supersaturation and nucleation at the liquid/solid interface initiating the crystal growth as seen in figure 2.1.

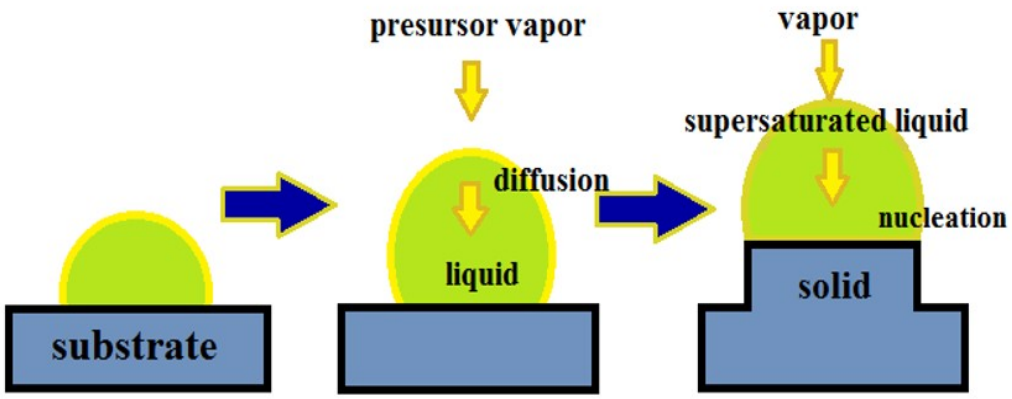

Fig 2.1. Growth of 1D structures by VLS mechanism

It is preferable to have the liquid droplet spread out in a very thin layer instead of remaining in droplet form, and this phenomenon is known as wetting [11]. The wettability depends mainly of

the surface free energy of the liquid and solid surface, interfacial energy between them, solubility and effects of diffusion between the two.

2.3.1 SPREADING OF LIQUID METALS ON SOLID SURFACES.

With our great interest to grow III-V materials through the VLS mechanism, it is important to focus on the spreading of liquid metals on solid surfaces. A comprehensive theory as derived by Harkins is mentioned here. Surface energy is defined as the work required to move the molecules from the bulk to the surface as to cover one square centimeter with them [13]. The free surface energy or surface tension of a substance is expressed as in equation 2.0 [13]

$$\gamma = \left(\partial F / \partial A\right) \tag{2.0}$$

where F is the free energy of the substance and A is the surface area at constant temperature, pressure and concentration. The condition for wettability to occur is defined as dF < 0. Two common relationships based on Law of Eötvos and Ramsay and Shields variation are used to predict the surface tension of molten metal [13].

$$\gamma\left(\frac{M}{\rho}\right)^{2/3} = K(T_c - T) \quad \text{and} \quad \gamma\left(\frac{M}{\rho}\right)^{2/3} = K(T_c - T - 6) \tag{2.1}$$

In equation 2.1 γ is the surface tension, M is the molecular weight, ρ is the density, T_c is the critical temperature and *K* is a constant Bikerman [14] has developed a relationship based on thermodynamics, which relates the surface tension of a liquid to its heat of vaporization derived from surface energy. The total surface energy including the heat effects can be expressed as

$$U_s = \gamma - \frac{\partial \gamma}{\partial T} T \tag{2.2}$$

While incorporating the area occupied by the molecule in the surface, the equation can be modified as

$$A\left(\gamma - \frac{\partial \gamma}{\partial T} T\right) = \frac{\Delta H_{vap} - RT}{N} \quad (2.3)$$

For isometric molecules, the area A is proportional to $(M/\rho N)^{2/3}$, the final equation is expressed as

$$\left(\frac{M}{\rho N}\right)^{\frac{2}{3}} \left(\gamma - \frac{\partial \gamma}{\partial T} T\right) = \frac{\Delta H_{vap} - RT}{N} \quad (2.4)$$

The surface tension of Indium is calculated to be [15]

$$\left(\frac{M}{\rho N}\right)^{2/3} \left(\gamma - \frac{\partial \gamma}{\partial T} T\right) = \frac{\Delta H_{vap} - RT}{N} \quad (2.5)$$

where t_{mp} is the melting point in ºC.

2.4 METHODS OF CHARACTERIZATION

The characterization techniques employed in this thesis for the analysis of the results are x-ray diffraction (XRD), spectroscopic ellipsometry (SE), scanning electron microscopy (SEM), imaging using an optical microscope and X-ray fluorescence (XRF). During this study, these techniques were used to find the thickness, roughness, crystallinity, composition, and location of the structure under study. A brief description of these methods is found below.

2.4.1 X-RAY DIFFRACTION (XRD)

X-ray diffraction is a powerful non-destructive technique used to analyze the important

characteristics of thin films such as the crystallographic structure, the crystallites orientation, crystal defects, grain size and other structural parameters based on their diffraction pattern. X-rays generated by a cathode ray tube and filtered to produce monochromatic radiation, are directed towards the surface of the sample. The material of the sample causes diffraction of the x-rays at various angles based on its crystal structure. The spectrum of diffracted samples are collected and plotted as a function of 2θ. The resultant peaks for diffraction are obtained. As every crystal has a unique structure, lattice constant and symmetry, all these parameters affect the diffraction angle, the number of peaks and the intensity of the diffraction. The crystal orientation, symmetry and the phase can be obtained by simply comparing the peaks with the X-ray diffraction database. Equation 2.6 gives the inter-planar spacing, $d_{hkl,}$ respective to each diffraction line, where λ is the wavelength of the X-ray radiation and θ is Bragg's angle of diffraction [20].

$$d_{hlk} = \frac{\lambda}{2Sin\theta} \tag{2.6}$$

The size of the crystallite can be predicted using Scherrer's formula given by equation 2.2

$$L = \frac{Ks\,\lambda}{\beta cos\theta} \tag{2.7}$$

where K_S is the Scherrer constant, L is the grain size, β is the full width at half maximum of the peak in radians, 2θ is the peak position and λ is the wavelength of the X-ray beam.

2.4.2 SPECTROSCOPIC ELLIPSOMETRY (SE) MEASUREMENT

SE is a non-destructive optical characterization technique that has been used to characterize the optical properties of thin film materials and devices. Ellipsometry is an optical measurement technique that measures the changes in the state of polarization of the light upon interaction

(reflection or transmission) with the material. The orientation and phase of the field vectors or the corresponding light wave are represented by the polarization of light. Due to the high sensitivity of the system, the polarization of the interacting light wave can change with even so small as a monolayer change in thickness. The advantage of modern fast computers is their ability to record these minute changes, which can be used for analysis, in the thickness.

Interaction of the Light with Material

When the light interacts with a material, the Maxwell's equations should be satisfied at all times. The interaction of light with the materials can be well described using a complex parameter which consists of two values used to describe the optical properties of the material. The complex index of refraction is given as

$$\tilde{n} = n + ik \tag{2.8}$$

'n' is called the index of refraction and 'k' is the extinction coefficient.

The optical properties can also be represented as a complex dielectric function given as:

$$\tilde{\varepsilon} = \varepsilon_1 + i\varepsilon_2 \tag{2.9}$$

The complex dielectric function can be related with the index of refraction with the following convention,

$$\tilde{\varepsilon} = \tilde{n}^2 \tag{2.10}$$

The index describes the phase velocity of light as it travels in a material compared to the speed of light in vacuum, *c*:

$$v = \frac{c}{n} \tag{2.11}$$

The velocity of the light reduces when it enters a material with higher index. The frequency of

the light remains as a constant; thus, the wavelength will shorten. In an absorbing medium, the decrease in intensity I per unit length z is proportional to the intensity. According to Beer's law [21],

$$I(z) = I_0 e^{-\propto z} \tag{2.12}$$

where I_0 is the value of the intensity at the surface of the absorbing medium.

The extinction coefficient describes the loss of wave energy to the material and is defined as [3]

$$\alpha = \frac{4\pi k}{\lambda} \tag{2.13}$$

When the light beam is incident on a material, the light will reflect and refract at the interface as shown in Figure 2.4.2. According to the law of reflection, the angle between the incident ray and normal (i) will be equal to the reflected (r). Figure 2.2 indicates the reflection and refraction of a light entering a medium using Snell's law. The light entering the material is refracted at an angle (ϕ) given by equation [6]

$$n_0 \sin(\Phi_i) = n_1 \sin(\Phi_i) \tag{2 .14}$$

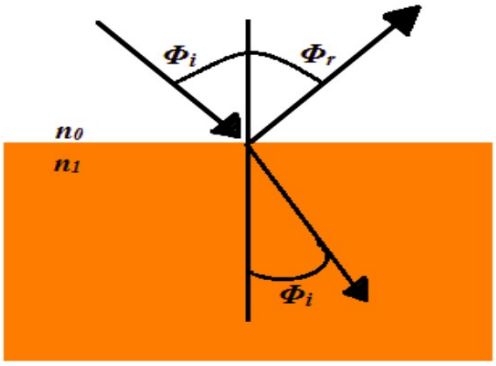

Fig 2.2. Light reflects and refracts in accordance to Snell's law

2.4.3 SCANNING ELECTRON MICROSCOPY (SEM)

Scanning electron microscopy (SEM) is an imaging technique used to view the grain size, grain boundaries and thickness of the different layers in a structure. The scanning electron microscopy utilizes a high-energy electron beam in a raster-scan. The raster-scan can be used to collect many signals from the three-dimensional surface of sample to be characterized and produces a highly-magnified image. A SEM consists of an electron gun, an electron lens system, an electron collector, electron detectors, display and recording devices and scanning coils. A larger magnification of the image is made possible as a result of the electron wavelength being much smaller than that of the wavelength of a photon, and a larger field of view is possible since the electron beam is small. This makes it possible to obtain a three-dimensional study of a specimen's surface.

The operation principle of a SEM is as follows. The focused electrons interact with the atoms in the specimen producing several different types of signals, which contain data about the specimen's surface morphology, composition, and other physical and chemical properties. The induced signals by an SEM include secondary electrons, back-scattered electrons (BSE), characteristic X-rays, photons as well as specimen current and transmitted electrons. Electrons with energies 0-30 eV are detected and used to form the image in secondary electron mode. These electrons are knocked out from within a few nanometers of the surface of the specimen. Backscattered electrons are electrons from the electron beam that are elastically scattered back from the sample and provides the information about the bulk properties of the materials since such scattering takes place in a volume extending down to 0.5 μm below the surface of the specimen.

2.4.4 X-RAY FLUORESCENCE (XRF)

XRF spectroscopy has broad applications in industry as well as in scientific research. XRF is a non-destructive, powerful elemental analysis based technique. The technique can be used to determine the elemental composition of a material. Most elements in the periodic table from boron to uranium can be identified or determined in the range of parts per million (ppm) to 100%. The working principle consists of bombarding a sample with primary X-rays that causes the constituent atom to be energized so that individual electrons move out of their normal positions and into orbitals further from the central nucleus. When the atom returns back to its stable state, the electrons drop back into their inner orbits and give off their excess energy in the form of characteristic secondary X-rays (fluorescence) whose energy is the difference between the two binding energies of the corresponding shells. By measuring the energies of the characteristic secondary X-rays, and counting the number of X-rays of each energy, XRF identifies the elements present in the sample and determines the relative concentration of these elements within the sample. The K and L shells are involved in XRF detection for most of the samples. A typical x-ray spectrum from an irradiated sample will display multiple peaks of different intensities. XRF can also be used for thickness measurement for films that are not thicker than the penetration depth of radiation.

CHAPTER 3

MODIFICATION OF INDIUM DEPOSITION PROCESS AND OF THE MULTILATER STRUCTURE

3.1 STUDY OF VARIOUS DEPOSITON TECHNIQUES

The various experimental techniques discussed in this research are very important for high-quality polycrystalline material. In this work the three physical vapor deposition (PVD) methods employed are 1) sputtering, 2) electron beam evaporation and 3) thermal evaporation. The Physical Vapor deposition is a collective set of processes used to deposit thin layers of materials, typically in the range of few nanometers to several micrometers.

3.1.1 Sputtering Deposition

Sputtering is a process in which when the surface of a target material is bombarded with high energy particles or ions atoms from the surface are ejected/dislodged. This causes a collision between the incident energized particles or the resultant recoil atoms, with the surface atoms. Each individual atom acquires sufficient energy individually and as the momentum of the incident ion is transferred to the atoms in the target material, due to the collision process, it allows the atoms to escape from the surface. Then the incident ion undergoes a series of collisions creating a set of other recoiling atoms. The sputtering process can be discussed in four basic steps: (1) Plasma generation, (2) Ion bombardment, (3) sputtered atom transport, and (4) film growth. The four stages are discussed in detail as follows [7, 8].

Plasma generation**:** Plasma generation is a crucial stage and should be monitored carefully. When an electric field is applied between the electrodes an ‘electron’ is generated which

accelerates towards the positively charged anode and acquires sufficient energy to ionize gas atoms upon collision to generate a glow discharge. To ionize the background gas to create plasma more electrons are generated as an avalanche effect is created. This results in the glow discharge. The positively charged ions created in the plasma get accelerated towards the target and lead to sputtering of the material.

Ion bombardment: In this stage, a transfer of momentum occurs from the positively charged ions generated to the target material and thereby this disrupts the surface at an atomic level. This could happen simultaneously with many atoms: when two atoms are struck simultaneously, most of the energy is transferred to the primary knock-on-atom and a small fraction of energy is transferred to the second atom. The primary knock-on atom creates a collision cascade in the surrounding atoms while the secondary atom transfers its energy to the surrounding atoms thus causing them to be ejected.

Sputtered atom transport**:** There are three modes of sputtered atom transport in the sputter deposition process, and they are determined by the background gas pressure. For the sputtered atom to be able to maintain its kinetic energy a low pressure (below 0.1 mTorr) is maintained. In an intermediate pressure (between 0.5 mTorr and 30 mTorr), the sputtered particles undergo more gas phase collisions. Most of the magnetron and RF diode sputter systems operate in this mode. The Sputter particles fully thermalize with the background gas and it is most common for most of the RF diode and all DC diode sputtering processes.

Film growth and properties: The sputtering species are ejected from the target in all directions and are deposited on the surrounding surfaces. The sputtered atoms are loosely condensed on

the bonded adatoms. The adatoms diffusion rate is dependent on the substrate material, its temperature and the influence of the substrate due to bombardment with energetic particles during growth. The higher energy adatoms may evaporate or sputter from the substrate surface, and adatoms with low mobility are absorbed onto the surface with low energy sites such as defects. Adatoms diffuse and coalesce into nuclei grown to form islands. These islands grow together to form a continuous film.

3.1.2 Electron beam Evaporation

Electron beam (E-beam) evaporation is a physical vapor deposition (PVD) technique whereby an intense electron beam is generated from a filament and steered via electric and magnetic fields to strike a source material (e.g. pellets of In) and vaporize it within a vacuum environment. At some point, as the source material is heated via this energy transfer, its surface atoms will have sufficient energy to leave the surface. At this stage, the surface atoms travel through the vacuum chamber, at a thermal energy of less that 1eV, and can be used to deposit on the substrate positioned above the evaporating material. The average working distances are from 300 mm to 1 meter. Since the thermal energy is low, a very low pressure of around 10^{-5} Torr or lower must be maintained. This is to make sure that the mean free path is longer than the distance between the electron beam source and the substrate [10].

3.1.3 Thermal Evaporation

Thermal Evaporation is one of the very common methods of PVD used for thin film deposition. This technology is used to coat the surface of various substrates with pure material. The thickness of the coating is in the range of angstroms to microns. A very important use of this

process is that the deposition could be of a single material or can be multiple materials in a layered structure [9]. The materials used with the thermal evaporation technique can be atomic elements of both metal and non- metals. Thermal evaporation involves heating a solid material inside a high vacuum chamber, taking it to a temperature that provides some vapor pressure. Inside the vacuum, even a relatively low vapor pressure is sufficient to raise a vapor cloud inside the chamber. This evaporated material now constitutes a vapor stream, which traverses the chamber and hits the substrate, sticking to it as a coating or film.

3.1.4 Deposition of Indium

Indium was deposited on different substrates using different deposition techniques. To compare the deposition processes, Indium was deposited on Mo foil by sputtering deposition, E- beam evaporation and Thermal Evaporation. The Mo foil was cleaned by consecutive rinses in acetone, isopropyl alcohol and deionized water at room temperature. The structure of the Indium film on Mo foil is depicted in Figure 3.1. The thickness of the film was kept constant at 400 nm for all the three deposition processes. E-beam evaporation was carried out in a Kurt Lesker PVD 75 machine with Indium pellets (99.999%, Alfa Aesar) at a vacuum of 4.8E-06 Torr. The rate of deposition was kept constant at 60 Å/s. Thermal Evaporation was carried out in a Kurt Lesker Thermal Co-evaporation system with Indium pellets (99.999%, Alfa Aesar) at a vacuum of 1.8 E-06 Torr. The deposition rate was kept constant at 2.5 Å/s. Sputtering deposition was carried out in a Kurt Lesker PVD 75 system with a 2” Indium sputtering target (Kurt Lesker) and the deposition rate was maintained at 2.7Å/s.

Fig 3.1(a). Schematic of the structure of Indium on Mo foil

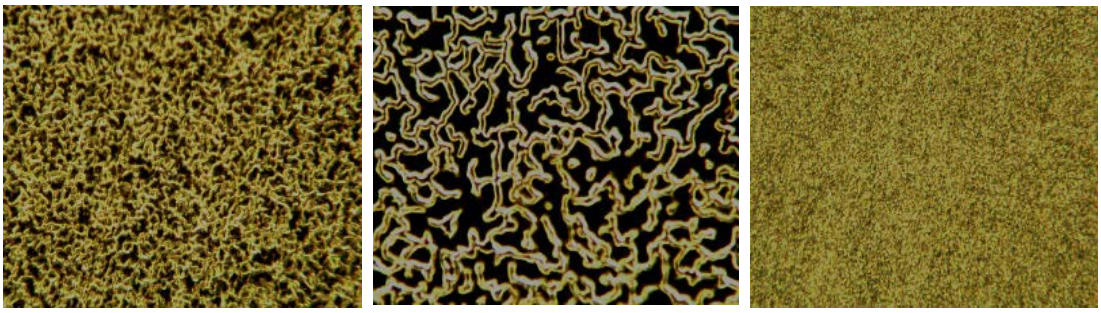

Fig 3.1(b). Optical images showing a comparison of Indium films deposited by E-Beam evaporation, Thermal Evaporation and Sputtering (Magnification X20)

Figure 3.1 compares the optical images of Indium film deposited by three different deposition processes. The Indium layer deposited by thermal evaporation fails to form a uniform layer and instead small islands are formed on the substrate. Better coverage is obtained with e-beam evaporation but still islands of Indium can be observed on the substrate. The best coverage was observed for the layer deposited using sputtering deposition, which shows that there is room for more study for the future. However, the duration of the sputtering process is much higher than the other two methods (3 hours versus 1 hour). Hence, for this study the focus was shifted to the E-beam method as it still has good surface coverage.

3.2 MODIFICATION OF THE MULTILAYER STRUCTURE

During the deposition of the Indium film, it is essential to obtain a uniform layer with uniform spreading of the film. De-wetting of Indium film is one of the major challenges faced during the deposition of this film. The de-wetting of the film is dependent on various factors like the free surface energy of the film and the substrate, the interfacial free energy between them etc. The

structure of film can be slightly enhanced by adding an additional layer to improve the wetting or the ability to spread of the film. Four different experiments were conducted to observe the changes in the coverage of In on the surface of the substrate.

3.2.1 Indium film on Soda lime glass substrate

In this experiment, a layer of In is deposited on a soda lime glass substrate. The Soda lime glass was cleaned using a concentrated micro soap solution added in a beaker filled with deionized (DI) water. The soda lime glass slides are soaked in the soap solution and agitated in a sonication bath at 60º C for 60 min. Then the glass slides were rinsed with DI water 3-4 times. The same process of sonication is done for 20-30 more min in clean DI water after which the slides are blown using dry nitrogen gas. The In film is deposited on SLG substrate by e-beam evaporation with a deposition rate of 60 Å/s. One can observed from the SEM image of In layer (Figure 3.2) that the In was not uniformly spread on the surface of the substrate but balled up.

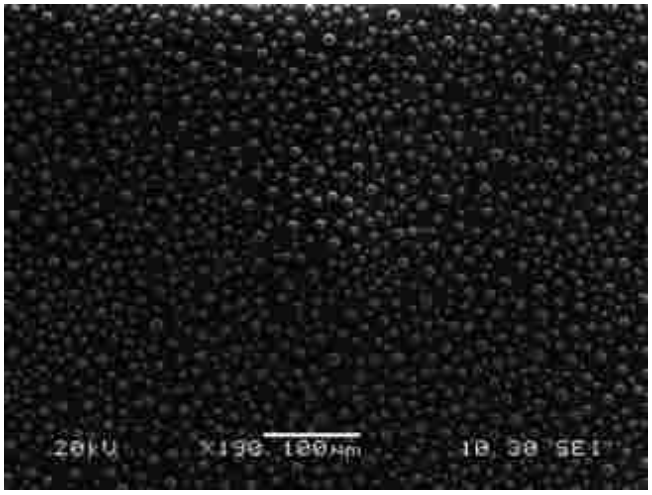

Figure 3.2 SEM image of In on SLG 190x

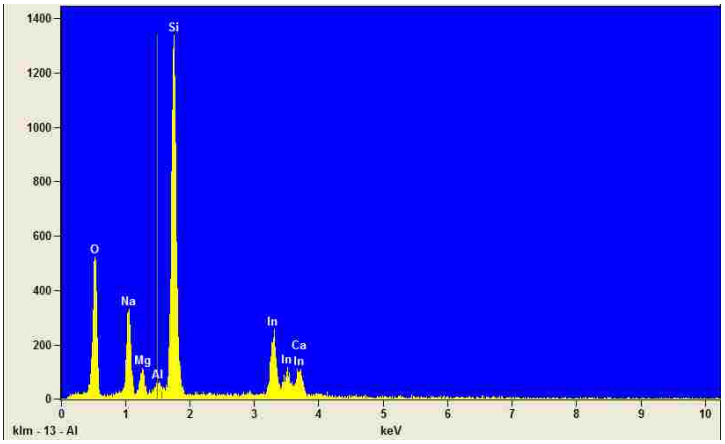

Fig 3.3. EDS Spectrum for In on SLG

Figure 3.3 shows the EDS spectrum of the elemental composition for the same structure. This shows high peaks of Si, O, and Na along with a small peak of In which proves that the deposition of Indium was not uniform and not as desired. The high peaks of Si, O, Na correspond to the substrate which is soda lime glass.

Element	*Weight %*	*Weight % Error*	*Norm. Wt.%*	*Norm. Wt.% Err*	*Atom %*	*Atom % Error*
O	0.76S	---	0.76S	---	1.65	+/- 0.03
Na	16.18	+/- 0.39	16.18	+/- 0.39	24.50	+/- 0.59
Mg	4.19	+/- 0.21	4.19	+/- 0.21	6.00	+/- 0.30
Al	0.86	+/- 0.15	0.86	+/- 0.15	1.10	+/- 0.19
Si	43.14	+/- 0.44	43.14	+/- 0.44	53.45	+/- 0.54
Ca	4.80	+/- 0.39	4.80	+/- 0.39	4.17	+/- 0.34
In	30.07	+/- 0.70	30.07	+/- 0.70	9.11	+/- 0.21
Total	100.00		100.00		100.00	

Table 3.1 EDS results of In on SLG

Table 3.1 summarizes the results of the EDS analysis. One can see that silicon has the highest

weight percentage followed by In. To analyze more precisely the local composition, some point analyses were done. The computer directs the electron beam to those areas and conducts the analysis. Figure 3.4 shows the points that were selected to be analyzed by the computer, which were the specific islands (1 and 2) and in between the islands (3). The scale marker indicates the length of 5 microns in the image.

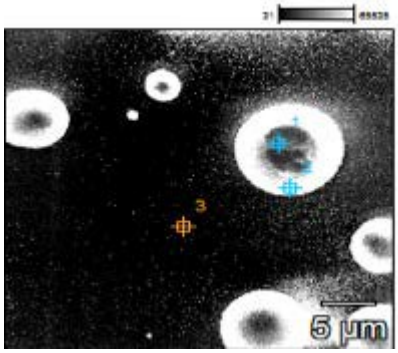

Fig 3.4. SEM image showing specific points of In on SLG to be analyzed

Figure 3.5 shows the EDS spectrum at point 1, which shows a strong Indium peak on the island,

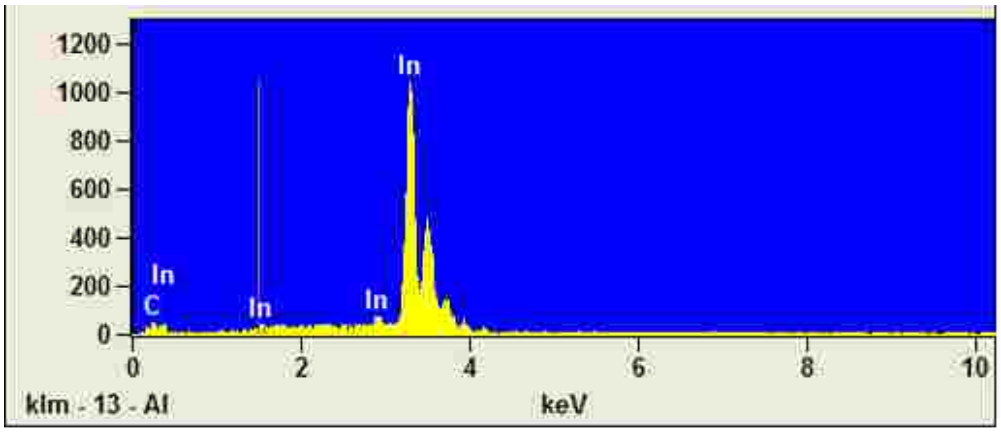

Fig 3.5 EDS spectrum of In on SLG point 1

which confirms the balling of In on the substrate.

Figure 3.6 shows the EDS spectrum at point 2, which again shows a strong Indium peak which confirms the balling of In on the substrate. Different peaks of Si and Na are also visible in this spectrum, which confirms the balling up of Indium as it focuses on the edge of the bubble and sees the substrate.

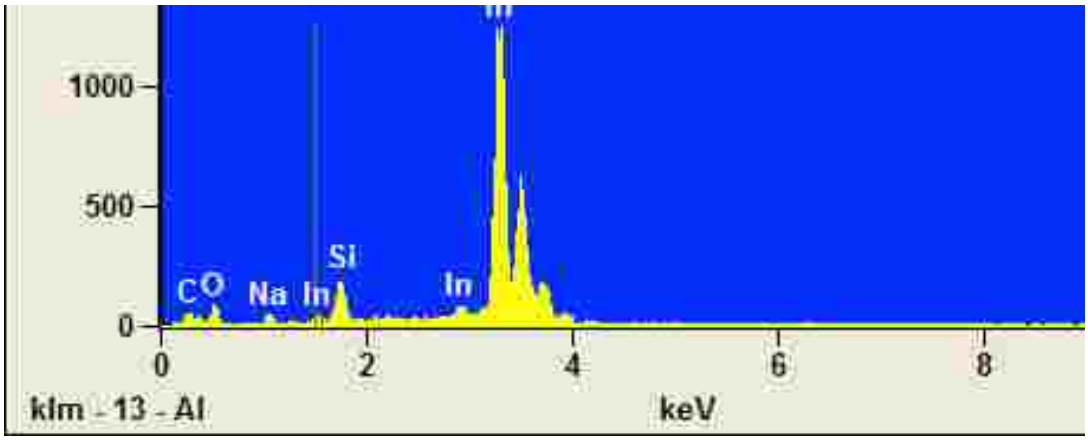

Fig 3.6 EDS spectrum of In on SLG point 2

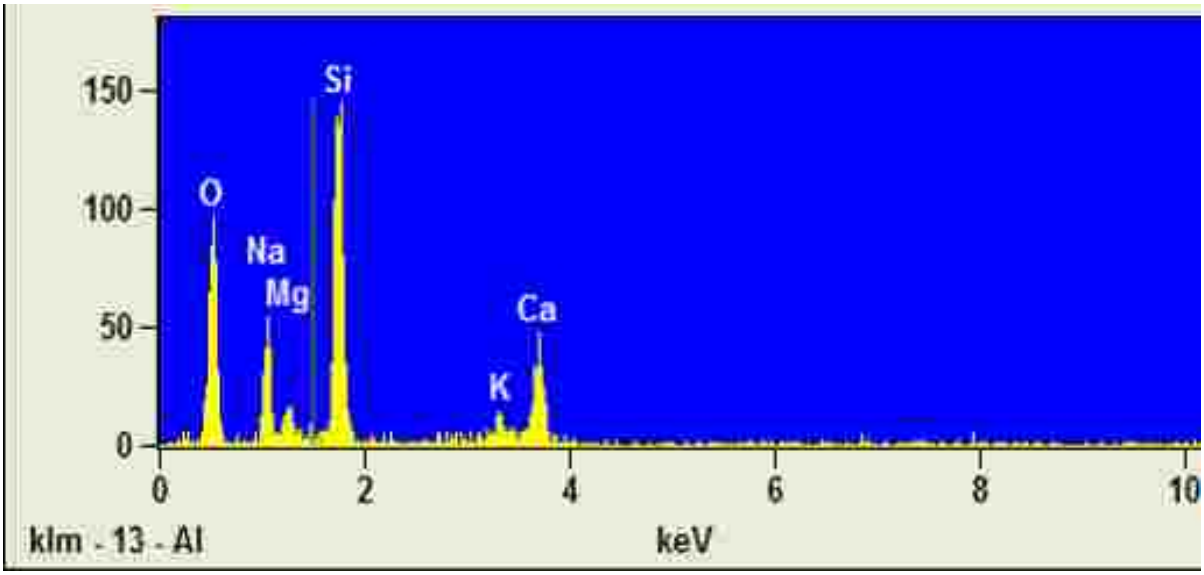

Fig 3.7. EDS spectrum image of In on SLG point 3

Figure 3.7 shows the EDS spectrum at point 3, which shows a strong Si peak but no Indium peak, which confirms that the In is not uniform throughout the surface of the substrate.

3.2.2 Indium film on Soda lime glass with Molybdenum layer

A layer of molybdenum was introduced between the Indium layer and the soda lime glass substrate. The Mo layer was deposited on a cleaned SLG substrate by sputtering deposition. The deposition was carried out in a Kurt Lesker PVD 75 machine with a 2” Mo target (99.9% Kurt Lesker) and the deposition conditions were adjusted to get a deposition rate of 2.7 Å/s. Indium was deposited by e-beam evaporation at a rate of 60 Å/s on the SLG/Mo substrate.

Figure 3.8 shows the SEM image and shows that the Indium is slightly more spread and not balling up as in the previous structure without the Mo layer.

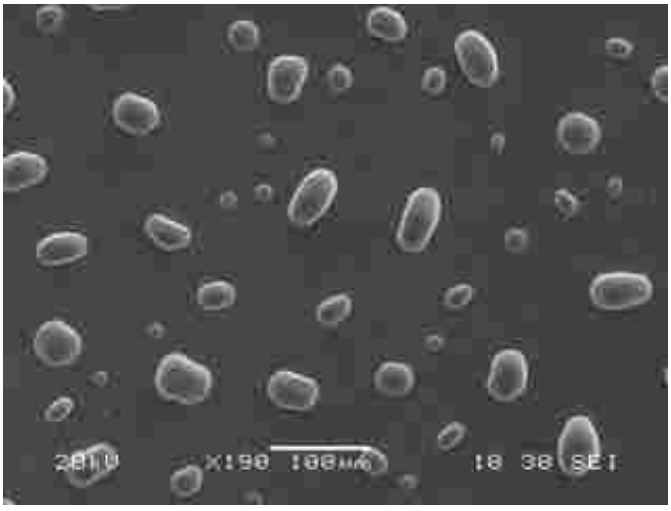

Fig 3.8 SEM image of In on SLG/Mo structure

Figure 3.9 shows the EDS spectrum with the elemental composition. This shows high peaks of Mo, along with a small peak of In, which proves that the deposition of Indium was not uniform and not as desired.

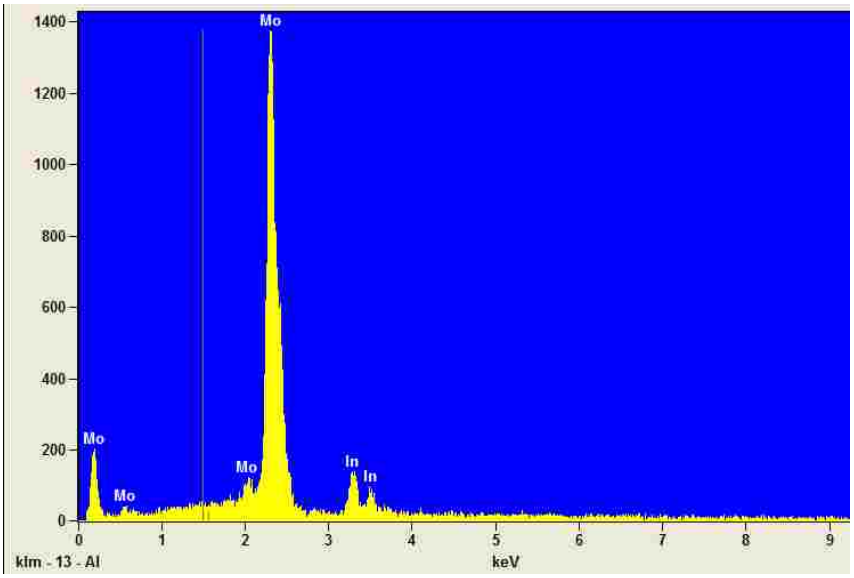

Figure 3.9 EDS Spectrum for In on SLG/Mo

Table 3.2 summarizes the results of the EDS analysis. The weight percentage of Mo is far more than that of the In as seen in the Table, indicating an incomplete coverage by In of the Mo.

Element	*Weight %*	*Weight % Error*	*Norm. Wt.%*	*Norm. Wt.% Err*	*Atom %*	*Atom % Error*
Mo	83.40	+/- 1.07	83.40	+/- 1.07	85.74	+/- 1.10
In	16.60	+/- 0.56	16.60	+/- 0.56	14.26	+/- 0.48
Total	100.00		100.00		100.00	

Table 3.2 EDS analysis of In on SLG/Mo

Figure 3.10 shows the two points that were selected to be analyzed by the computer. The scale marker indicates the length of 25 microns in the image. The first point selected is to be on the area with the white surface, which is supposedly In.

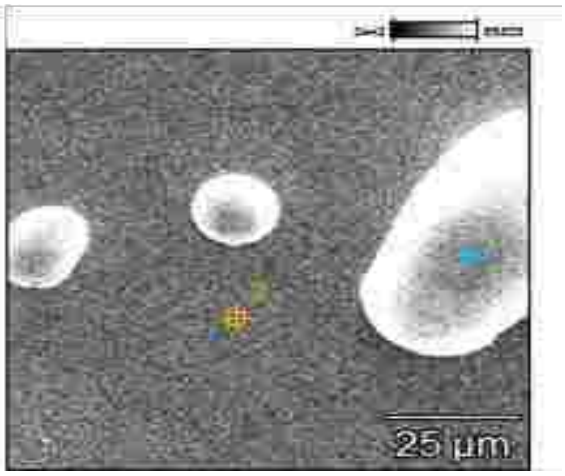

Fig 3.10 SEM image showing specific points of In
on SLG/Mo to be analyzed

Figure 3.11 shows the EDS spectrum at Point 1, which shows only a strong Indium peak, confirming that the islands are formed of Indium.

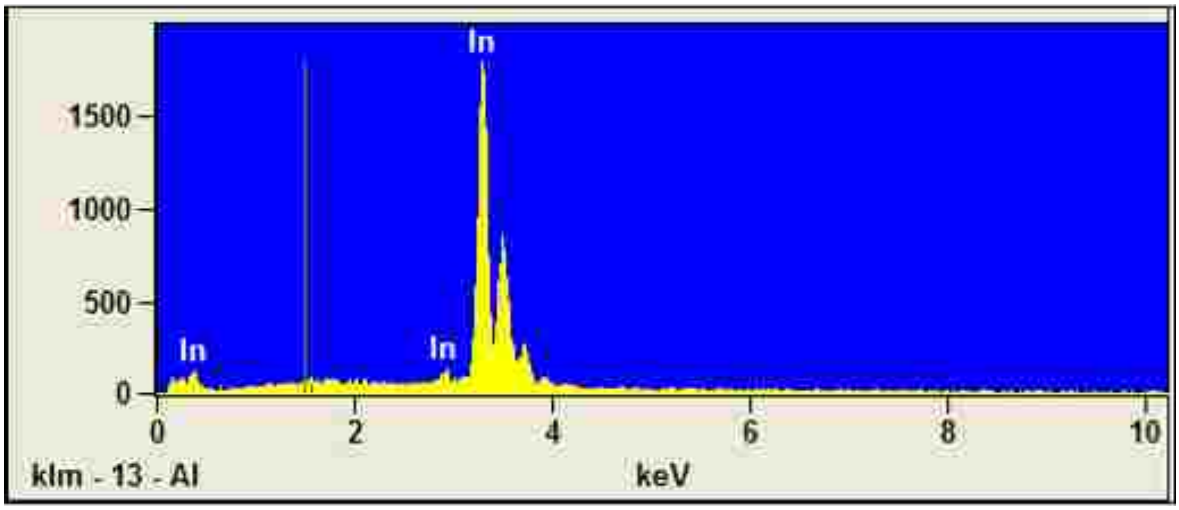

Fig 3.11 EDS spectrum image of In on SLG/Mo at Point 1

Figure 3.12 shows the EDS spectrum at Point 2, which shows a strong peak of Mo without any

trace of Indium, indicating that In is indeed segregated.

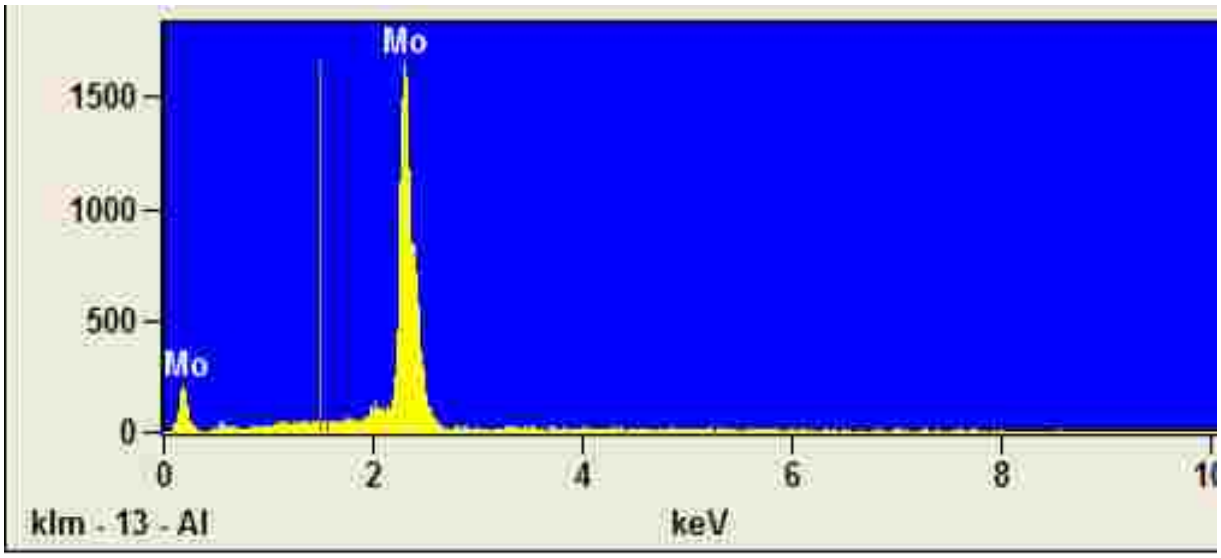

Fig 3.12 EDS spectrum of In on SLG/Mo at Point 2

3.2.3 Addition of a SiO_2 layer

A thin SiO_2 capping layer was introduced to prevent de-wetting of the Indium layer from the top interface. This layer enables the liquid Indium to maintain a planar geometry by preventing it from de-wetting [3]. Indium was first deposited on the surface of the SLG substrate by electron beam evaporation at 60 Å/s. After the deposition of Indium film, SiO_2 was deposited by electron beam deposition at a rate of 3 Å/s without breaking the vacuum.

Figure 3.13 is a SEM image of the surface of the structure. It shows that the Indium is still balled up but is more spread out than for the previous two experiments.

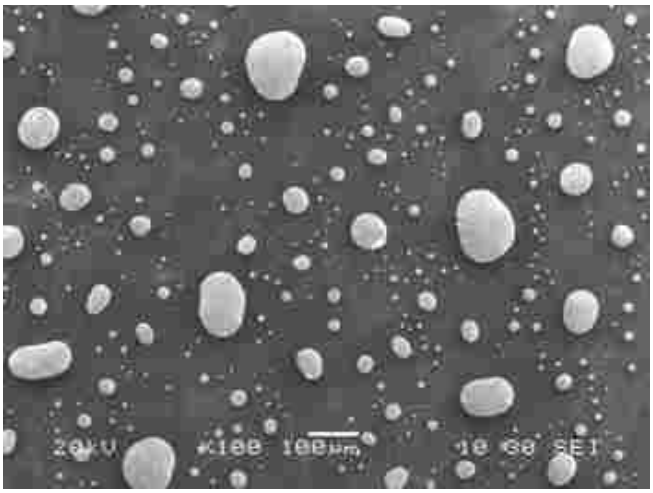

Fig 3.13. SEM image of Indium layer on SLG substrate with SiO_2 capping layer

Figure 3.14 shows the two points that were selected to be analyzed by the computer. The scale marker indicates the length of 100 microns in the image. The first point selected is to be on the

Figure 3.14 SEM image showing specific points of In on SLG with SiO_2 capping layer to be analyzed.

area with the white surface, which is supposed to be In. Figure 3.15 shows the EDS spectrum at Point 1 that shows a strong Indium peak, which confirms the presence of Indium on the substrate, and a Si peak corresponding to the SiO_2 capping layer.

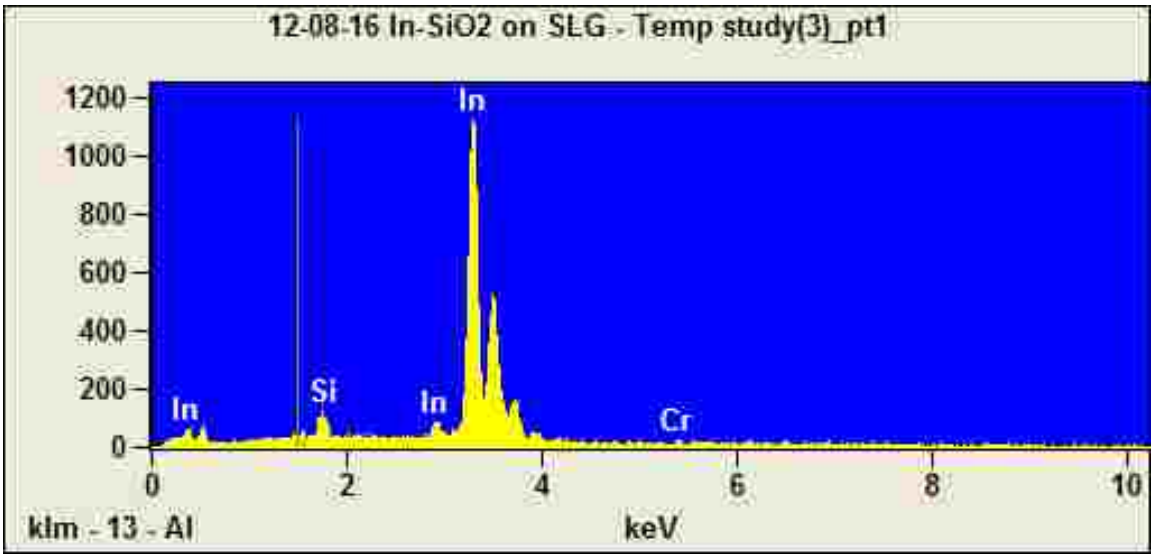

Fig 3.15. EDS spectrum of In on SiO_2 on SLG (Point 1)

Figure 3.16 shows the EDS spectrum at point 2, which shows a strong Si peak but no Indium peak, which confirm that In is not present at this location.

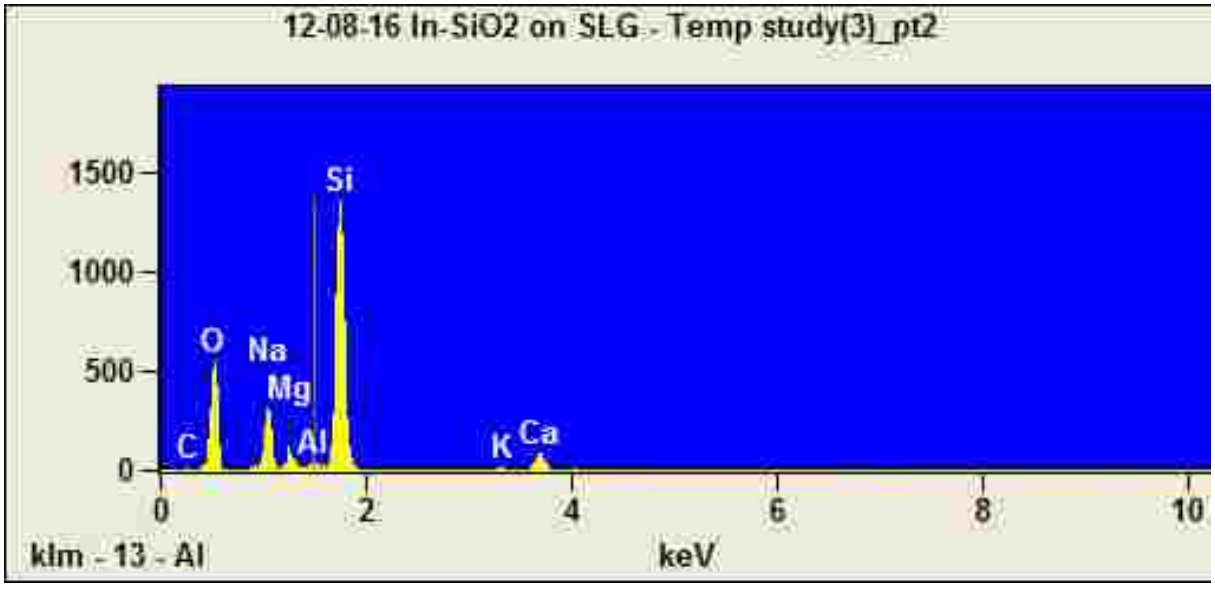

Fig 3.16 EDS spectrum of In with SiO_2 capping layer on SLG (Point 2)

3.2.3 Addition of SiO_2 layer on SLG substrate with Mo layer

The fourth experiment is a combination of the previous two experiments. First, a layer of Mo is deposited on the SLG substrate by sputtering at a rate of 2.7 Å/s. In is deposited on the surface of

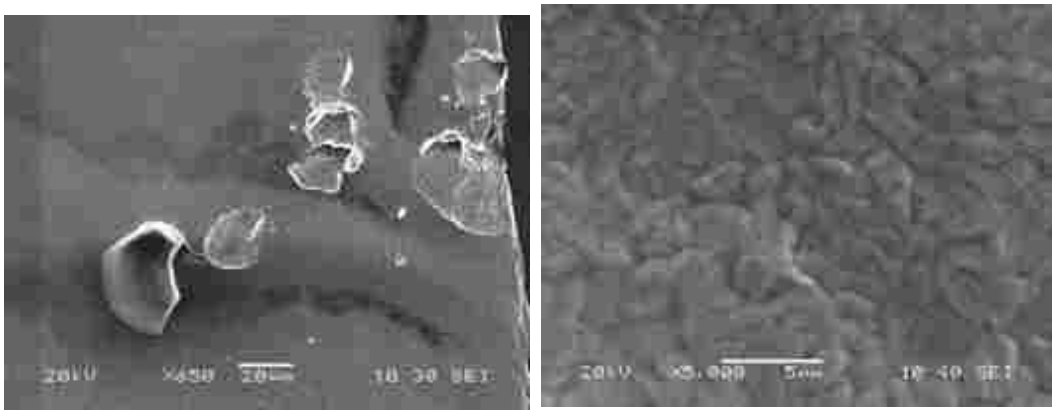

Fig 3.17 SEM image of In layer with SiO_2 capping on SLG/Mo substrate at magnifications of 190x and 5000x

the SLG/Mo by electron beam deposition at 60 Å/s. After the deposition of Indium, SiO_2 is deposited by electron beam deposition at a rate of 3 Å/s. Figure 3.17 shows the SEM image of the Indium layer with SiO_2 capping layer on SLG/Mo substrate. One can see that there is much more consistent spread of Indium on the surface of the substrate. In this case since the first image, which was optically enlarged 650 times, was not clear enough to figure out the spread of Indium on the surface, so a much more enlarged image was captured. Figure 3.17(b) captures an image that shows better coverage and uniform spread of the Indium layer on the substrate due to the presence of both the SiO_2 capping layer and Mo substrate. With the addition of the Mo layer, the interface properties are improved between the SLG substrate, and it helps in the wetting of the Indium layer on the substrate during deposition, while the SiO_2 capping layer prevents the de-

wetting from happening at the top interface.

Figure 3.18 shows the four points that were selected to be analyzed by the computer. The scale marker indicates the length of 5 microns in the image.

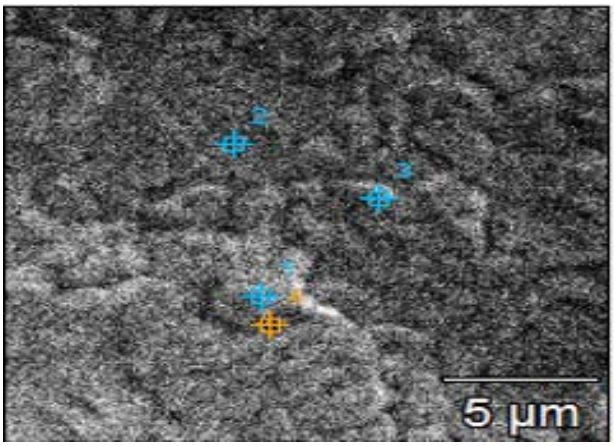

Fig 3.18 SEM image showing specific points of In on SLG/Mo with SiO_2 capping layer to be analyzed

Table 3.3 summarizes the results of the EDS analysis. The weight percentage of Mo is almost as much as the percentage of In, which clearly shows that the In is much more uniformly spread than the other experiments conducted.

Element	*Weight %*	*Weight % Error*	*Norm. Wt.%*	*Norm. Wt.% Err*	*Atom %*	*Atom % Error*
O	10.97	+/- 1.18	10.97	+/- 1.18	42.18	+/- 4.53
Si	3.20	+/- 0.11	3.20	+/- 0.11	7.01	+/- 0.24
Mo	45.54	+/- 0.66	45.54	+/- 0.66	29.21	+/- 0.42
In	40.29	+/- 0.70	40.29	+/- 0.70	21.60	+/- 0.38
Total	100.00		100.00		100.00	

Table 3.3 EDS analysis of In on SLG/Mo with SiO_2 capping

Figure 3.19 shows the EDS spectrum at Points 1 and 4, which shows strong In and Mo peaks, demonstrating the uniformity of both Mo and In. Analysis of Points 2 and 3 suggests that there is still a major portion of the substrate that does not have the deposition of In, which means that there is still room for improvement.

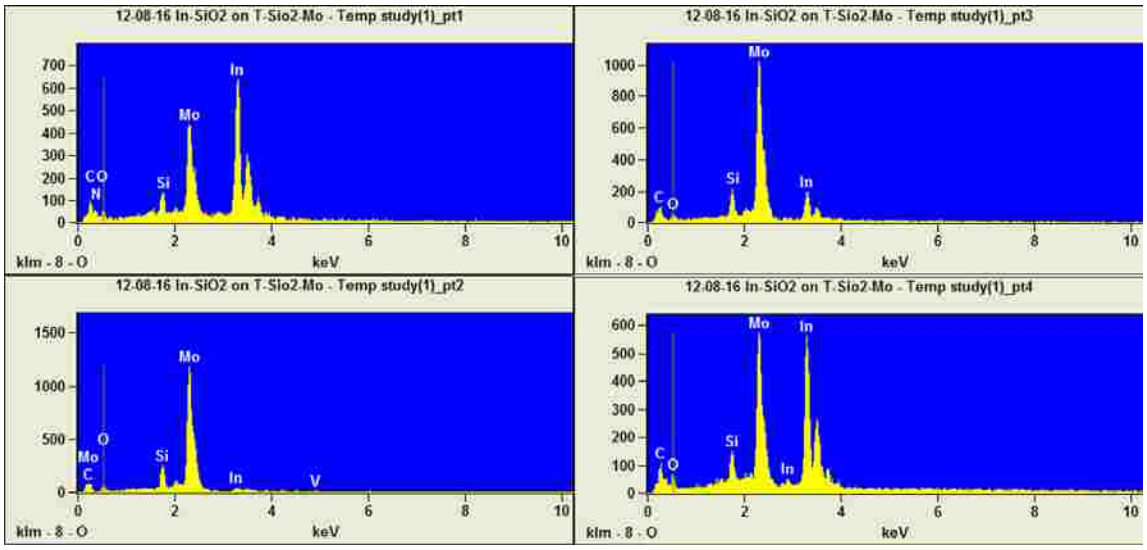

Fig 3.19 EDS spectrum for In layer with SiO_2 capping on SLG/Mo substrate for the 4 points of Figure 3.18

CHAPTER 4

STUDY OF THE UNIFORMITY AS A FUNCTION OF TEMPERATURE FOR DIFFERENT DEPOSITON RATES

4.1 MODIFYING THE DEPOSITION RATE OF INDIUM

Since the addition of Mo and SiO_2 layers in the previous chapter led to a much more uniform layer of In, a different approach was implemented. In the previous chapter, Indium layers were deposited by E-beam evaporation at 60 Å/s, which gave reasonable results. In this chapter, the deposition rate for Indium was varied, and the effect of deposition rate on the uniformity of the layer was observed. Mo foil was chosen as a substrate for this set of experiments. The Mo foil was cleaned using consecutive rinses in acetone, isopropyl alcohol and deionized water at room temperature. The thickness of the film was kept constant at 400 nm for all the three deposition rates. The three deposition rates were 2Å/s, 60Å/s and 100Å/s. E-beam evaporation was carried out in Kurt Lesker PVD 75 machine with Indium pellets (99.999%, Alfa Aesar) at a vacuum of 4.5E-06 Torr.

Figure 4.1 shows the SEM images of the samples with different rates of 2Å/s, 60Å/s and 100Å/s. The first image with a very low rate of 2Å/s shows the formation of islands. The Indium layer deposited at 60 Å/s (Figure 4.1b) shows that at this higher rate the In spreads better. The Indium layer deposited at a rate of 100Å/s (Figure 4.1c) displays a uniform and better coverage as compared to the previous two rates of deposition. Due to the significance of this result, the deposition rate of Indium was set to 100 Å/s for all further experiments.

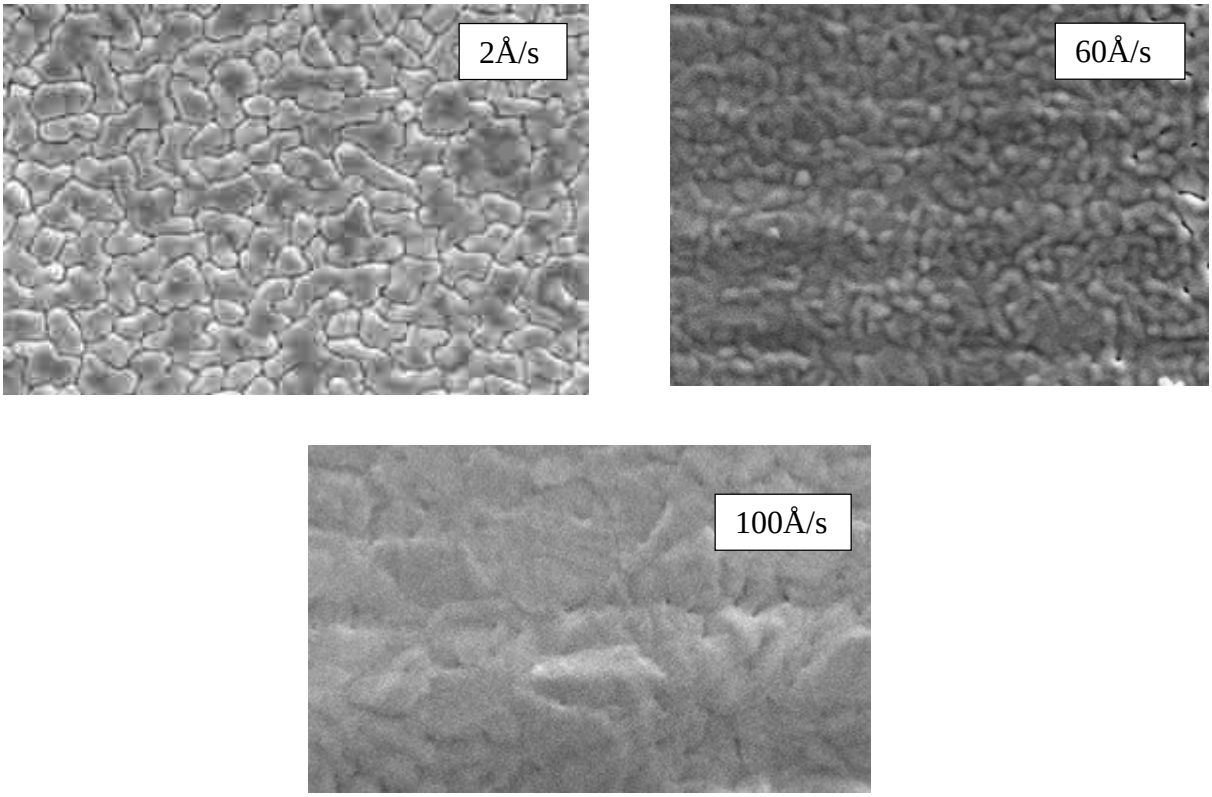

Fig 4.1 SEM image of In layer on Mo foil at 2 Å/s 60 Å/s 100 Å/s

4.2 MODIFYING THE DEPOSITION RATE OF SIO_2

The Indium layer deposited at a rate of 100 Å/s has been demonstrated to have better coverage on the substrate. Now to further increase the spreading of the Indium on the surface of the substrate more experiments were done to study the effect of SiO_2. The rate of deposition of SiO_2 was varied and deposited on different types of substrates. The substrates used were soda lime glass, silicon with native oxide (native Si), Mo foil and high temperature glass with sodium barrier (Tec SB). The samples were deposited on different substrates so as to study the influence of substrates on the wetting of Indium. The Mo foil was cleaned using consecutive rinses in acetone, isopropyl alcohol and deionized water at room temperature. The Soda lime glass was

cleaned using a concentrated micro soap solution added in a beaker filled with deionized (DI) water. The soda lime glass slides are allowed to soak in the soap solution and agitated in a sonication bath at 60º C for 60 min. Then these glass slides are rinsed with DI water 3-4 times. The same process of sonication is done for 20-30 more minutes in clean DI water after which the slides are blown using dry nitrogen gas. The cleaning method for Native Si is same as that of Mo foil. The samples were annealed at 200ºC in vacuum after the deposition to compare the effect on the structure of the Indium film with different deposition rates of SiO_2. This temperature was chosen as it is above the Indium melting point.

To begin with the experiments, a set of samples was first deposited with Mo deposited by either sputtering or E-beam evaporation. Sputtering was performed in a Kurt Lesker PVD 75 system with a 2" Molybdenum sputtering target (Kurt Lesker) and the deposition rate was maintained at 2.7Å/s. Mo was sputtered only on SLG and Native Si. Samples with a sputtered Mo layer are labeled as Mo–SP and samples. Mo layer deposited by e-beam evaporation were deposited on the same substrates and are labeled as Mo-EB.

After enough samples were generated, a set of samples could go through a series of three material depositions by electron beam evaporation method starting with a thin layer of Mo of 5 nm at a rate of 0.2 Å/s followed by a 1 micron layer of Indium at a rate of 100 Å/s and finally a layer of SiO_2 at one of the 4 different rates: 3Å/s, 5Å/s, 10Å/s and 15Å/s.

4.2.1 Deposition of SiO_2 at 3Å/s

Table 4.1 shows the deposition parameters, conditions and duration of the experiments. Figure 4.2(a) shows the optical image of Indium layer with SiO_2 capping layer on Native Silicon with a 5-nm thick Mo layer deposited by e-beam evaporation and Figure 4.2(b) shows the optical image

of Indium layer with SiO_2 capping layer on native silicon with a sputtered Mo layer and a thin Mo layer deposited by e-beam evaporation. Both these samples were annealed at 200°C under vacuum after the deposition. Comparing these two images, one can see that the sample which has the additional pre-deposited Mo layer by sputtering is much more uniform that the one without the sputtered Mo. with a 5-nm thick Mo layer deposited by e-beam evaporation.

Table 4.1 Experimental setup for sample with SiO_2 deposited at 3 *Å/s*

Sample ID : 03-02-17 In_Temp			
Substrates : SLG, Mo foil and NSi			
Deposition Parameter	**Mo Deposition (E-beam)**	**Indium deposition**	**Silicon dioxide deposition**
Base pressure of chamber	3.2E-06	4.4E-07	5.4E-07
Beam Voltage	8KV	8KV	8KV
Beam Current	85	25	4.5-5.5
Rate	0.07-0.12	100 A°/s	3 A°/s
Final thickness	5 nm	1.0 µm	50 nm
Total duration	55mins	24mins	8 mins

Fig 4.2 (a) Optical image of Indium layer with SiO_2 capping layer on Native Si/Mo-EB

Fig 4.2 (b) Optical image of Indium layer with SiO_2 capping layer on Native Si/Mo-SP/Mo-EB

Figure 4.3(b) shows the optical image of an Indium layer with SiO_2 capping layer on SLG with a pre-sputtered Mo layer and a thin Mo layer deposited by e-beam evaporation. Both these samples were annealed at 200° C under vacuum after the deposition.

There is a clear distinction between the two samples, as the sample with an additional sputtering.

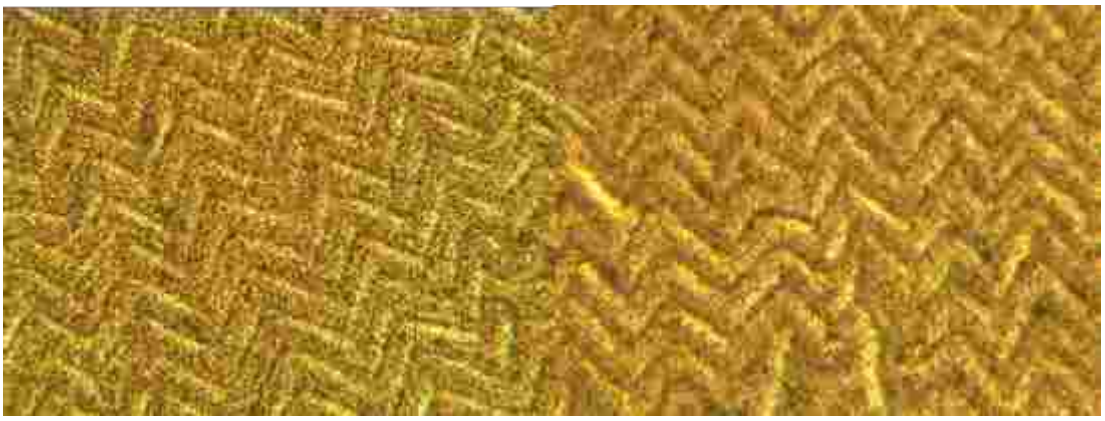

Fig 4.3(a) Optical image of Indium layer with SiO_2 capping layer on SLG/Mo-EB

Fig 4.3(b) Optical image of Indium layer with SiO_2 capping layer on SLG/Mo-SP/Mo-EB

Mo layer has slightly larger grain size when compared to the other.

Figure 4.4 shows the optical image of an Indium layer with SiO_2 capping layer on cleaned Mo foil with a 5-nm thick Mo layer deposited by e-beam evaporation.

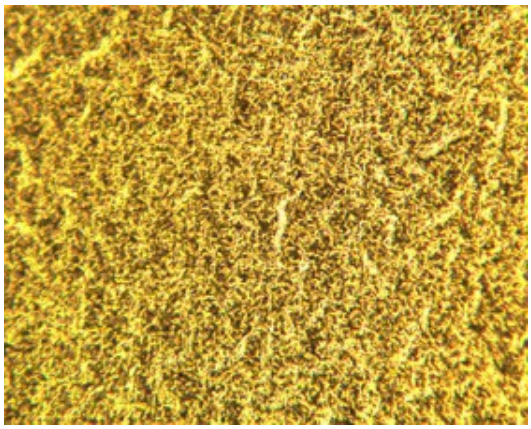

Fig 4.4 Optical image of Indium layer with SiO_2 capping layer on Mo foil/Mo-EB

Here also the film is quite uniform even though it has a finer structure.

4.2.2 DEPOSITION OF SIO_2 AT 5Å/s

Table 4.2 shows the deposition parameters, conditions and duration of the experiments. The rate of deposition of SiO_2 was changed to 5Å/s. Figure 4.5(a) shows the optical image of Indium layer with SiO_2 capping layer on Native Silicon with a 5-nm thick Mo layer deposited by e-beam evaporation and Figure 4.5(b) shows the optical image of Indium layer with SiO_2 capping layer on native silicon with a sputtered Mo layer and a thin Mo layer deposited by e-beam evaporation. Both these samples were annealed at 200°C under vacuum after the deposition. Comparing these two images we see that the sample which has the additional pre-deposited Mo layer by sputtering is much more uniform that the one without the sputtered Mo.

Table 4.2 Experimental setup for sample with SiO_2 deposited at 5 *Å/s*

Sample ID : 03-08-17 In_Temp InT002			
Substrates :SLG, Mo foil and NSi			
Deposition Parameter	**Mo Deposition (E-beam)**	**Indium deposition**	**Silicon dioxide deposition**
Base pressure of chamber	3.2E-06	1.8E-06	1.9E-06
Beam Voltage	8KV	8KV	8KV
Beam Current	83-85	31-33	9.11 mA
Rate	0.09-0.14	100 A°/s	5 A°/s
Final thickness	5 nm	1.0 µm	50 nm
Total duration	39mins	23mins	5 mins

Fig 4.5(a) Optical image of Indium layer with SiO_2 capping layer on Native Si/Mo-EB

Fig 4.5(b) Optical image of Indium layer with SiO_2 capping layer on Native Si/Mo-SP/Mo-EB

The same experiment was repeated on SLG substrates. Figure 4.6 (a) shows the optical image of an Indium layer with SiO_2 capping layer on SLG with a 5-nm thick Mo layer deposited by e-beam evaporation and Figure 4.6 (b) shows the optical image of an Indium layer with SiO_2 capping layer on SLG with a pre-sputtered Mo layer and a thin Mo layer deposited by e-beam evaporation. Both these samples were annealed at 200° C under vacuum after the deposition. There is better uniformity and better coverage with the predeposited Mo layer.

Fig 4.6(a) Optical image of Indium layer with SiO_2 capping layer on SLG/Mo-EB

Fig 4.6(b) Optical image of Indium layer with SiO_2 capping layer on SLG/Mo-SP/Mo-EB

Figure 4.7 shows the optical image of an Indium layer with SiO_2 capping layer on Mo foil with a 5-nm thick Mo layer deposited by e-beam evaporation. Unlike the previous images (Figure 4.4), the de-wetting of Indium is more prominent on Mo foil.

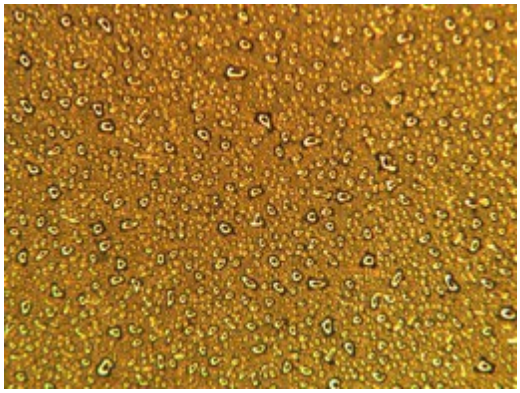

Fig 4.7 Optical image of Indium layer with SiO_2 capping layer on Mo foil/Mo-EB

4.2.3 DEPOSITION OF SIO_2 AT 10Å/s

Table 4.3 Experimental setup for sample with SiO_2 deposited at 10 *Å/s*

Sample ID : 03-09-17 In_Temp			
Substrates : SLG, Mo foil and NSi			
Deposition parameters	**Mo Deposition (E-beam)**	**Indium deposition**	**Silicon dioxide deposition**
Base pressure of chamber	7.3E-06	1.2E-06	2.9E-06
Beam Voltage	8KV	8KV	8KV
Beam Current	79-81	40-42	8-12
Rate	0.09-0.11	100 A°/s	10 A°/s
Final thickness	5 nm	1.0 µm	50 nm
Total duration	34 mins	19mins	7 mins

Table 4.3 shows the deposition parameters, conditions and duration of the experiments. The rate of deposition of SiO_2 was changed to 10Å/s. Figure 4.8 (a) shows the optical image of an Indium layer with SiO_2 capping layer on Native Silicon with a 5 nm thick Mo layer deposited by e-beam evaporation and Figure 4.8 (b) shows the optical image of an Indium layer with SiO_2 capping layer on native silicon with a sputtered Mo layer and a thin Mo layer deposited by e-beam

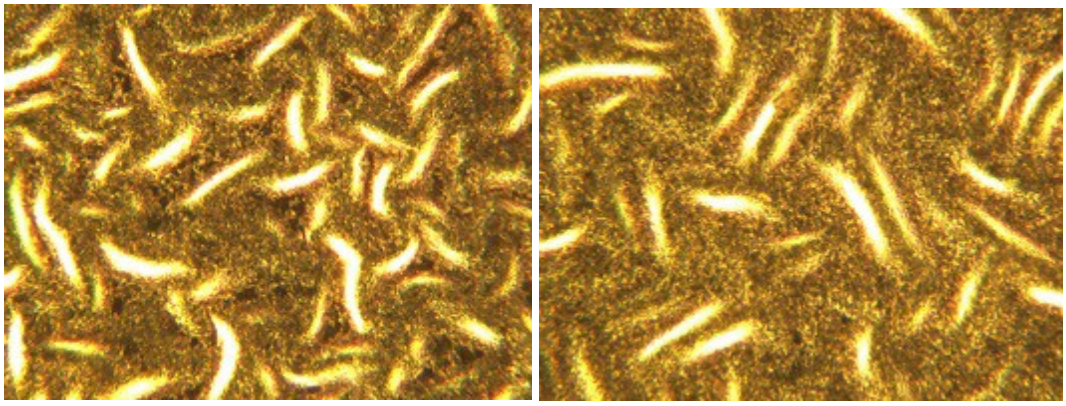

Fig 4.8 (a) Optical image of In layer with SiO_2 capping layer on Native Si/Mo-EB

Fig 4.8 (b) Optical image of In layer with SiO_2 capping layer on Native Si/Mo-SP/Mo-EB evaporation. Both these samples were annealed at 200° C under vacuum after the deposition.

Unlike the previous images (Figure 4.5) there is less coverage of Indium on the substrates in both cases. The same experiment was repeated on SLG substrates. Figure 4.9 (a) shows the optical image of an Indium layer with SiO_2 capping layer on SLG with a 5-nm thick Mo layer deposited by e- beam evaporation and Figure 4.9 (b) shows the optical image of an Indium layer with SiO_2 capping layer on SLG with a pre-sputtered Mo layer and a thin Mo layer deposited by e-beam evaporation and both these samples were annealed at 200° C under vacuum after the deposition. There is definitely better uniformity and smoother grains with the layer with pre-deposited Mo layer.

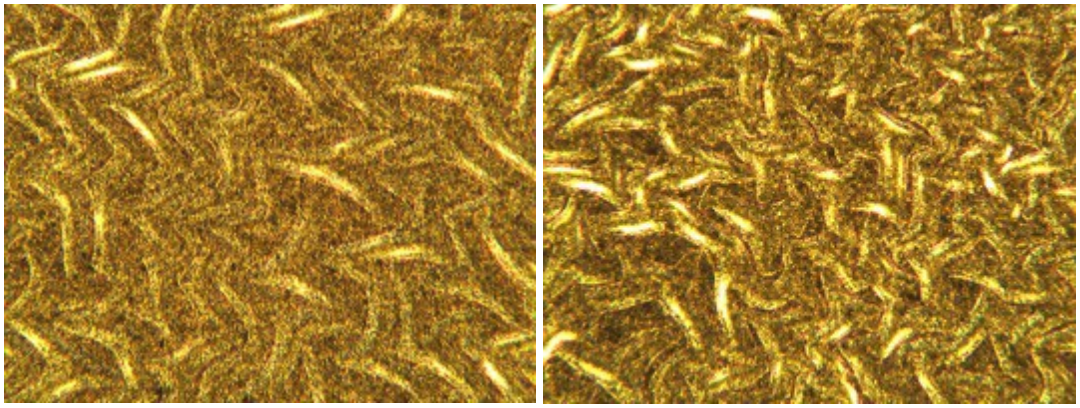

Fig 4.9 (a) Optical image of Indium layer with SiO_2 capping layer on SLG/Mo-EB

Fig 4.9 (b) Optical image of Indium layer with SiO_2 capping layer on SLG/Mo-SP/Mo-EB

Fig 4.10 shows the optical image of an Indium layer with SiO_2 capping layer on Mo foil with a 5-nm thick Mo layer deposited by e-beam evaporation. Unlike the previous images (Figure 4.7), the de-wetting of Indium is more prominent on Mo foil.

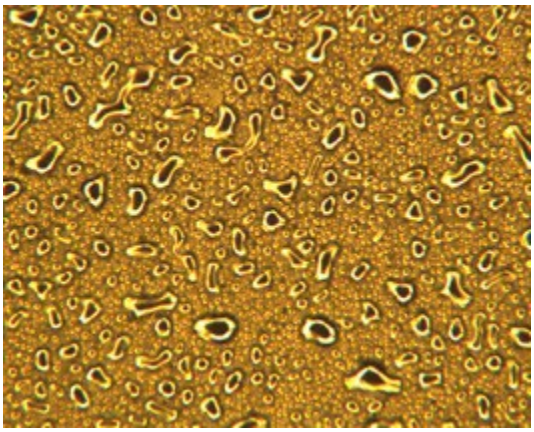

Fig 4.10 Optical image of Indium layer with SiO_2 capping layer on Mo foil/Mo-EB

4.2.4 DEPOSITION OF SIO_2 AT 15Å/s

Table 4.4 shows the deposition parameters, conditions and duration of the experiments. The rate

of deposition of SiO_2 was changed to 15Å/s. Figure 4.11 (a) shows the optical image of an Indium layer with SiO_2 capping layer on Native Silicon with a 5-nm thick Mo layer deposited by e-beam evaporation and Figure 4.11 (b) shows the optical image of an Indium layer with SiO_2 capping layer on native silicon with a sputtered Mo layer and a thin Mo layer deposited by e- beam evaporation. Both these samples were annealed at 200° C under vacuum after the deposition. Unlike the previous images (Figure 4.8), there is less coverage of Indium on the substrates. However, for the samples with a pre-deposited Mo layer, the islands seem to have better coverage and have bigger grain size.

Table 4.4 Experimental setup for sample with SiO_2 deposited at 15 Å/s

Sample ID : 03-11-17 In_Temp			
Substrates : SLG, Mo foil and NSi			
Deposition Parameters	**Mo Deposition (E-beam)**	**Indium deposition**	**Silicon dioxide deposition**
Base pressure of chamber	8.8E-07	1.8E-06	1.4E-06
Beam Voltage	8KV	8KV	8KV
Beam Current	43-45	40-41	15-19
Rate	0.19-0.26	100 A°/s	15 A°/s
Final thickness	5 nm	1.0 µm	50 nm
Total duration	18mins	12mins	9 mins

The same experiment was repeated on SLG substrates. Figure 4.12 (a) shows the optical image of an Indium layer with SiO_2 capping layer on SLG with a 5-nm thick Mo layer deposited by e-

beam evaporation and Figure 4.12 (b) shows the optical image of an Indium layer with SiO_2 capping layer on SLG with a pre-sputtered Mo layer and a thin Mo layer deposited by e-beam evaporation. Both these samples were annealed at 200° C under vacuum after the deposition. Unlike the previous images (Figure 4.9), there is less coverage of Indium on the substrates. There is not much difference between the two samples with a pre-deposited Mo layer on SLG.

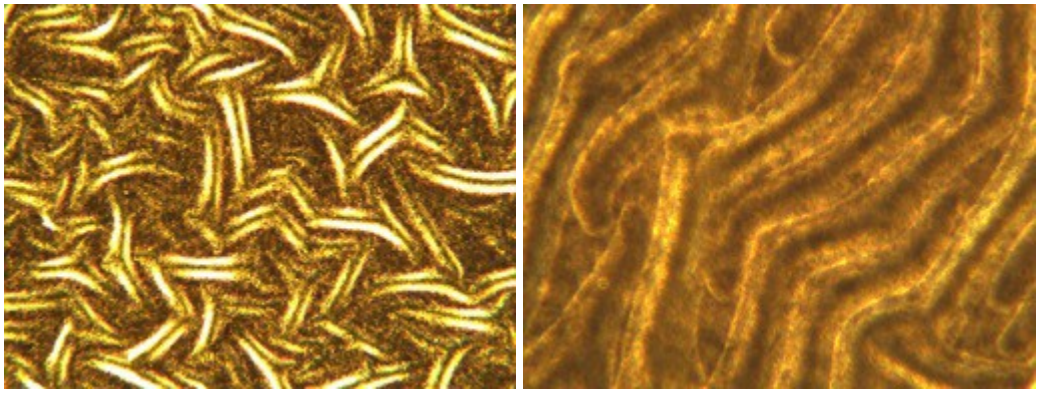

Fig 4.11 (a) Optical image of In layer with SiO_2 capping layer on Native Si/Mo-EB

Fig 4.11 (b) Optical image of In layer with SiO_2 capping layer on Native Si/Mo-SP/Mo-EB

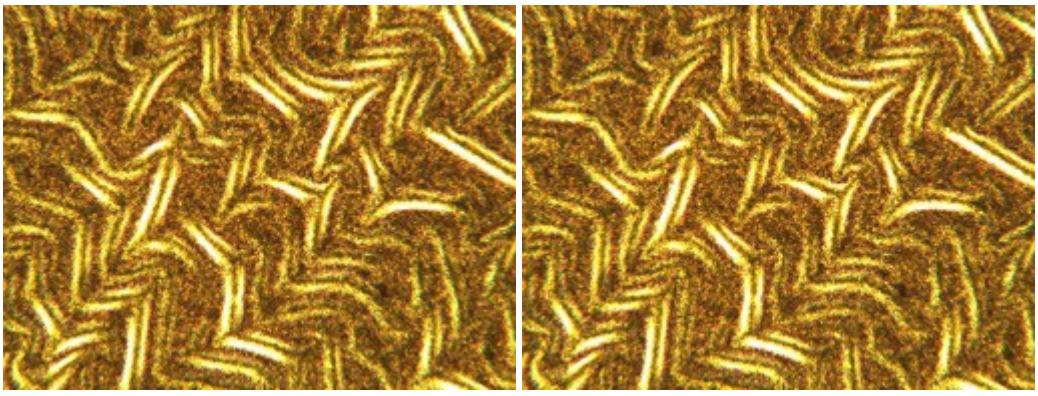

Fig 4.12 (a) Optical image of Indium layer with SiO_2 capping layer on SLG/Mo-EB

Fig 4.12 (b) Optical image of Indium layer with SiO_2 capping layer on SLG/Mo-SP/Mo-EB

Figure 4.13 shows the optical image of an Indium layer with SiO_2 capping layer on Mo foil

with a 5-nm thick Mo layer deposited by e-beam evaporation. Unlike the previous images (Figure 4.7), the de-wetting of Indium is more prominent on Mo foil and there are fewer islands of

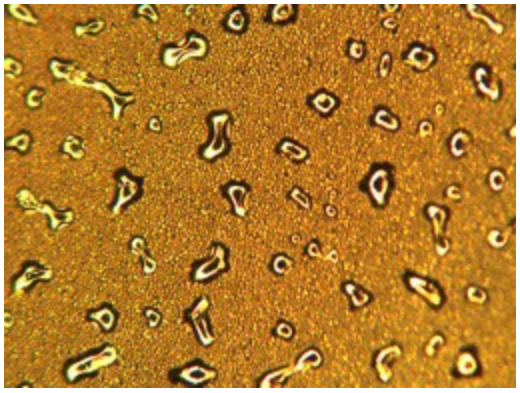

Fig 4.13 Optical image of Indium layer with SiO_2 capping layer on Mo foil/Mo-EB

Indium on the substrate. While comparing the different images obtained from the Optical microscope, samples with a SiO_2 layer deposited at a slower rate (3Å/s) seem to be of higher quality in terms of uniformity when compared to the layer deposited at 15Å/s. With the higher rate of deposition, there is a change in the density of the layer, which affects the porosity. The change in porosity and density of the layer can affect the interfacial energy between the Indium and SiO_2 layer, which might modify the surface energy and prevent a uniform spreading of the Indium layer.

4.3 SPECTROSCOPIC ELLIPSOMETRY ANALYSIS

In the previous section, the rate of deposition of the SiO_2 layer was varied, and the uniformity and coverage of the films were analyzed using an optical microscope. The samples with different SiO_2 layer, with native silicon substrate, were further analyzed using spectroscopic ellipsometry. With the change in the structure dimension, the mechanical and optical properties of the bulk

layer may be affected. An attempt has been made to obtain a relationship between the refractive index n and the density of the SiO_2 layers deposited at different deposition rates.

The spectral characteristics of ψ (ratio of amplitudes after reflection for polarizations p and s) and Δ (phase change after reflection for polarizations p and s) were obtained from spectroscopic ellipsometry [3]. A mathematical model was created based on the actual structure with specified thicknesses. A Cauchy dispersive model was used to fit ellipsometric data for dielectrics and semiconductors in spectral regions where they are transparent (extinction coefficient, k=0). The model allows determining the optical coefficients and thickness of the analyzed layers of the structure. The Cauchy dispersive formula is given by [2]

$$n(\lambda) = A + \frac{B}{\lambda^2} + \frac{C}{\lambda^4} + \cdots$$

where A, B, C are fitting coefficients and λ is the wavelength is μm.

Figure 4.14 shows the variation in refractive index, n, for the SiO_2 layers deposited with different deposition rates. It is clearly evident that the refractive index varies with the deposition rates.

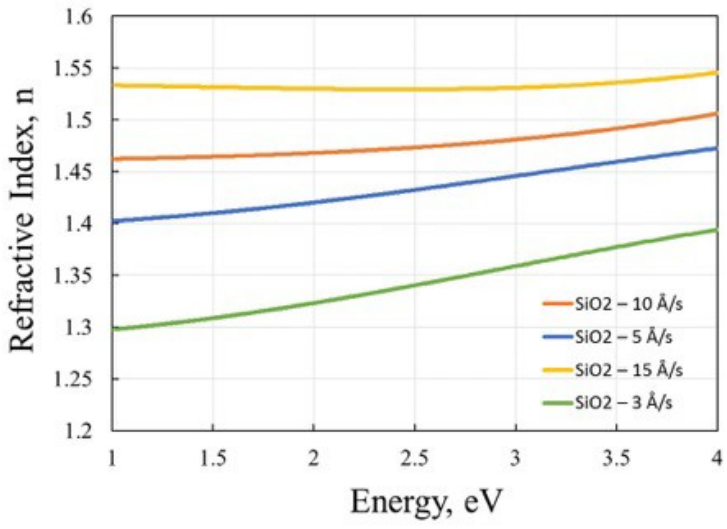

Fig 4.14. Refractive index as extracted by SE as a function of SiO_2 deposition rates

The increase of the refractive index of the oxide film features an increase in the packing density of the film [4]. This is well illustrated by the optical images as obtained from the optical microscope in the previous section.

4.4 XRF ANALYSIS

XRF analysis was performed to obtain a qualitative analysis of the intensity of Indium in the samples. When an electron beam of high energy strikes the sample, it displays the interaction of the emission of photons having a broad continuum of energies [17]. The raw data provides the number of counts of element – specific fluorescent X-ray energies received by the detector and it is visualized in a spectrum graph. The spectrum graph represents the element specific fluorescent energies in the x-axis and the intensity or counts in the y-axis. The peaks in the spectrum corresponds to the detection of element specific fluorescent energies and the higher the peak, the more counts of the particular energy was detected.

Two samples were chosen with an Indium layer with SiO_2 capping layer on a SLG substrate with a pre-sputtered Mo layer and a thin Mo layer deposited by e-beam evaporation [18]. Sample A had an SiO_2 capping layer deposited by e-beam evaporation at a rate of 3 Å/s and sample B with an SiO_2 capping layer deposited by e-beam evaporation at a rate of 15 Å/s. Fig 4.15(a) shows the XRF analysis of the In layer with SiO_2 capping layer deposited at 3 Å/s and Fig 4.15(b) shows the XRF analysis of the In layer with SiO_2 capping layer deposited at 15 Å/s. It is clearly evident that sample B has a higher In count when compared to sample A. The SiO_2 layer deposited at a higher deposition rate might have a higher packing density which has been confirmed by SE analysis (Fig 4.14). This probably affects the surface tension of the layer and the interfacial energy at the In/SiO_2 interface. This has clearly affected the increased de-wetting of the layer at

higher deposition rate and can be confirmed by the optical images obtained in Fig 4.12 [19].

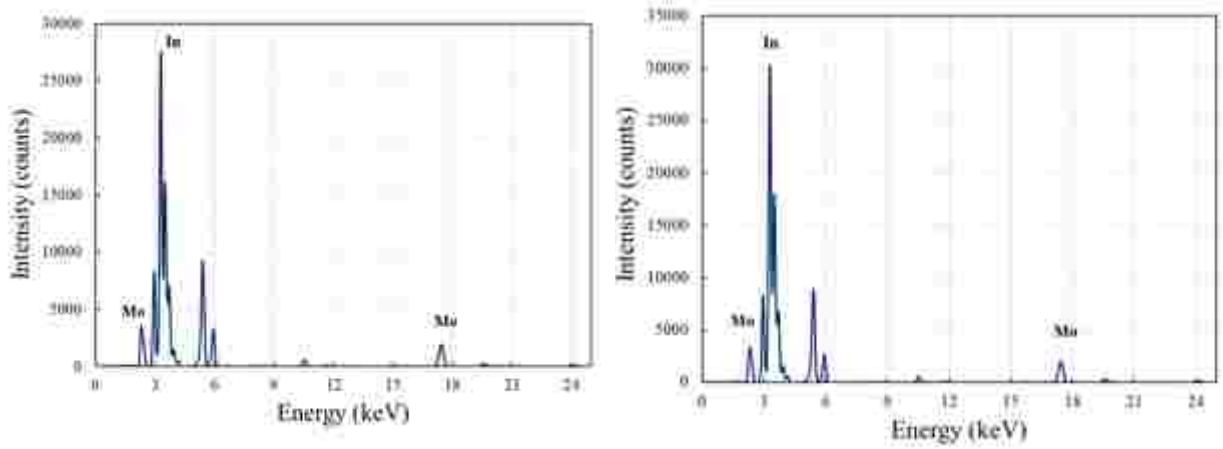

Fig 4.15 (a) XRF analysis of In layer with SiO_2 capping layer deposited at 3 Å/s Fig 4.15 (b) XRF analysis of In layer with SiO_2 capping layer deposited at 15 Å/s

CONCLUSION

III-V materials can be used for high efficiencies single and multi-junction cells and awide variety of optoelectronic devices. However, the cost of the III-V materials is extremely high due to the cost of the raw materials, the need for a lattice-matched substrate for single crystal growth and complex growth processes. In an attempt to grow III-V materials directly on cheaper substrates like Mo foil and SLG substrates by VLS growth, it is important to develop a planar reaction template for the group III metal that will prevent de-wetting of the seed layer from the substrate during growth. Considering the parameters and the different techniques that could be used to be able to grow an III-V material, experiments were conducted to grow a uniform layer of Indium so as to prepare a groundwork to fabricate InP, InAs, InN and InSb. Different deposition processes and structures were optimized to achieve the best uniform growth.

Three stages of experiments were conducted to be able to achieve uniform growth of Indium on various substrates. The growth mechanism of In was studied by carefully analyzing characterizations in the early growth stages as well as later. Three methods of deposition were tested to obtain a more uniform layer of Indium. Out of the three processes of e-beam evaporation, sputtering and thermal evaporation, the e-beam evaporation was found to be more reliable with a higher deposition rate and lower cost compared to the sputtering deposition.

Further experiments were conducted to analyze the effects of the growth of Indium with the change in deposition rate from 2Å/s, 60Å/s to 100Å/s. The best results were obtained, as substantiated by SEM images, for an In layer grown on Mo foil with a rate of deposition of 100Å/s. For the later experiments the rate of Indium was kept constant at 100Å/s.

The use of Mo as an additional layer by sputtering was tested, and it was observed that the addition of Mo helped achieve a uniform layer of In on the surface of the substrate. Before the deposition of the In layer by e-beam, a thin Mo layer of 5 nm was deposited on the substrate. This additional Mo layer aids in attaining more uniformity due to the change in the interfacial energy between the substrate and the In layer. The same set of experiments was conducted with and without an additional layer of SiO_2 (deposited by e-beam evaporation). It was demonstrated that this SiO_2 layer enhanced the spread of Indium. These samples were characterized with the help of scanning electron microscope and EDS spectrum to analyze the composition of the elements on the substrates and to ensure the uniformity of Indium. The final experiment was conducted to analyze the effect of change in the rate of deposition of SiO_2. Several experiments were conducted with the rate of SiO_2 (deposited by e-beam evaporation) changed from 3Å/s, 5Å/s, 10Å/s to 15Å/s. The images, obtained by an optical microscope for these experiments, showed that the most uniform In layer with minimal de-wetting was obtained with a SiO_2 capping layer deposited at a rate of 3Å/s. Spectroscopic ellipsometry was used to extract the optical constants of the different SiO_2 layers to obtain a better understanding of the structural and optical properties of the layer, showing that the density of the SiO_2 layer was changing with the deposition rate. XRF analysis was also carried out to obtain a qualitative analysis of the different samples.

REFERENCES

[1] R. Kapadia et al., "A direct thin-film path towards low-cost large-area III-V photovoltaics," *Scientific reports*, vol. 3, p. 2275, 2013.

[2] M. Zheng et al., "High optical quality polycrystalline Indium phosphide grown on metal substrates by metalorganic chemical vapor deposition," *Journal of Applied Physics*, vol. 111, no. 12, p. 123112, 2012.

[3] J. P. Connolly and D. Mencaraglia, "III–V Solar Cells," ed: Royal Society of Chemistry, 2014.

[4] G. Phipps, C. Mikolajczak, and T. Guckes, "Indium and gallium: long-term supply," *Renewable energy focus*, vol. 9, no. 4, pp. 56-59, 2008.

[5] A. P. Levitt, Whisker technology. John Wiley & Sons, 1970.

[6] H.-J. Choi, "Vapor–liquid–solid growth of semiconductor nanowires," in *Semiconductor Nanostructures for Optoelectronic Devices: Springer*, 2012, pp. 1-36.

[7] P. Sigmund, "Theory of sputtering. I. Sputtering yield of amorphous and polycrystalline targets," *Physical review*, vol. 184, no. 2, p. 383, 1969.

[8] N. Williams and J. Cuomo, "Sputter Deposition," *Wiley Encyclopedia of Electrical and Electronics Engineering*, 2003.

[9] R. F. Bunshah, *Handbook of deposition technologies for films and coatings: science, technology, and applications*. William Andrew, 1994.

[10] T. M. Adams and R. A. Layton, *Introductory MEMS: fabrication and applications.* Springer Science & Business Media, 2009.

[11] K. L. Osborne III, "Temperature-dependence of the contact angle of water on graphite, silicon, and gold," Worcester Polytechnic Institute, 2009.

[12] D. Sageman and G. Burnet, "Predicting the surface tension of liquid metals," *Journal of Inorganic and Nuclear Chemistry*, vol. 36, no. 5, pp. 1105-1107, 1974.

[13] A. Bondi, "The Spreading of Liquid Metals on Solid Surfaces. Surface Chemistry of High-Energy Substances," *Chemical Reviews*, vol. 52, no. 2, pp. 417-458, 1953.

[14] E. Paleolog, A. Fedotova, O. Derjagina, and N. Tomashov, "Anodic Process Kinetics on the Passive Surfaces of Titanium, Nickel, and Titanium-Nickel Alloys," *Journal of The Electrochemical Society*, vol. 125, no. 9, pp. 1410-1415, 1978.

[15] C. Suryanarayana and M. G. Norton, X-ray diffraction: *a practical approach*. Springer Science & Business Media, 2013.

[16] W. Rzodkiewicz and A. Panas, "Determination of the analytical relationship between refractive index and density of SiO2 layers," *Acta Physica Polonica A*, vol. 116, no. S, 2009.

[17] W. Rzodkiewicz, A. Kudla, A. Misiuk, and S. Lasisz, "Spectroscopic ellipsometry investigation of influence of high-pressure high-temperature process on optical properties of SiO2-Si structures," *in Lightmetry*, 2001, pp. 134-139: International Society for Optics and Photonics.

[18] A. González-Elipe, F. Yubero, and J. M. Sanz, *Low energy ion assisted film growth*. World Scientific, 2003.

[19] V. E. Buhrke, R. Jenkins, D. K. Smith, and D. Kingsley, *Practical guide for the preparation of specimens for x-ray fluorescence and x-ray diffraction analysis*. Wiley-VCH, 1998.

[20] C. Suryanarayana and N. Grant, "A Practical Approach Plenum Press," *New York*, 1998.

VITA

Isaac Butt

231 Kaufman Hall
ECE Department
Old Dominion University
Norfolk, VA 23529

Education

2017 M.S.	Electrical Engineering	Old Dominion University
2014 B.Tech	Electronics and communication	Jawaharlal Nehru Technological University, India